2025 SUMMER PROGRAMS at CNF

:: FINAL REPORTS ::

TABLE of CONTENTS

Characterization of Silicon Carbide Wafers

CNF Summer Student: Tyrone Chen
Student Affiliation: Department of Material Science and Engineering , Cornell University College of Engineering

Summer Program(s): 2025 Cornell NanoScale Facility Research Experience for Undergraduates (CNF REU) Program
Mentor(s): Phil Infante, Cornell NanoScale Science and Technology Facility, Cornell University
Primary Source(s) of Research Funding: National Science Foundation under Grant No. NNCI-2025233,
Contact: tc724@cornell.edu, pi12@cornell.edu
Summer Program Website(s): https://cnf.cornell.edu/education/reu

Abstract:

This project focused on characterizing silicon carbide (SiC) thin films deposited using low pressure chemical vapor deposition (LPCVD). The films were grown from a mixture of dichlorosilane (DCS) and acetylene (C_2H_2) gas, with hydrogen gas as the carrier gas aiding deposition, at two deposition temperatures: 800°C and 850°C. To help isolate the electrical properties of the SiC layer itself, two types of substrates were used—plain silicon wafers and silicon wafers with a deposited layer of silicon oxide. All wafers were cleaned using a standard MOS process and loaded into the A4 SiC furnace for deposition, where the ratio of DCS to acetylene was systematically varied. After deposition, the films were analyzed for thickness, refractive index, intrinsic stress, and resistivity. A noticeable drop in stress or refractive index at certain gas ratios suggested a potential change in film crystalline structure In the final phase, ammonia (NH_3) was introduced during deposition to explore in-situ doping. Some of these doped films showed unexpectedly low stress and very high conductivity. One particular sample could not be accurately modeled using standard optical fitting tools, suggesting an unusual film structure or electronic behavior. While more work is needed, these results point toward new ways to engineer SiC films with customized electrical and mechanical properties.

Summary of Research:

This project focused on the low-pressure chemical vapor deposition (LPCVD) of silicon carbide (SiC) thin films using dichlorosilane (DCS) and acetylene (C_2H_2) gas. This work aimed to investigate the effects of deposition conditions—specifically gas ratios and temperature—on film characteristics such as thickness, refractive index, stress, and resistivity, with the broader goal of tailoring SiC films properties for potential semiconductor applications. A secondary goal was to explore the effect of ammonia (NH_3) doping on electrical and mechanical properties. The wafers used for deposition included both bare silicon wafers and silicon wafers with deposited silicon oxide layers. The oxide-coated wafers served to isolate the electrical properties of the SiC film by minimizing current leakage into the substrate. Prior to deposition, all wafers underwent a cleaning sequence beginning with a sodium hydroxide (NaOH) base bath, followed by a rinse, then an acid bath using hydrochloric acid (HCl), and a final rinse until the surface resistivity reached approximately 16 MΩ·cm. These wafers were then spun dry and ready for depositions. This surface preparation ensured minimal contamination and enabled consistent film growth.

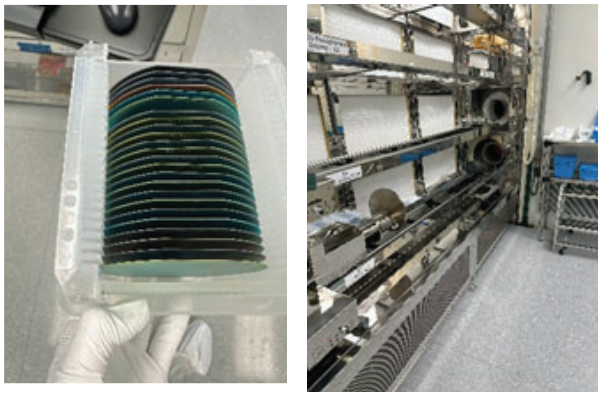

Figure 1: The picture on the right shows the furnace that was used for the deposition process. The picture on the left shows the resulted wafers that were deposited. As you can see the color of the wafers are an indicator of the thin film and this color may vary depending on the deposition conditions.

Deposition was carried out in the A4 SiC furnace under low-pressure conditions. The precursor gases—200 sccm of DCS and 50 sccm of acetylene had varying ratios where the DCS was kept at 31% max sccm while the acetylene ranged from 38% - 22% max sccm, while hydrogen was introduced as a helping gas. The hydrogen flow was found to be essential for achieving uniform films; wafers processed without it displayed black spots and non-uniform coverage. Depositions were performed at two temperatures: 800 °C and 850 °C. At 850 °C, deposition time was held around 70 minutes, while at 800 °C the process time was extended to approximately 140 minutes. These times were chosen to target a final film thickness of about 130 nm. Pressure within the furnace was actively controlled through a series of automated sequences including purging,

pump-down, leak checking, and venting.
After deposition, multiple characterization techniques were used to assess the films. The RC Woollam ellipsometer was first used to measure the thickness and refractive index from the reflective surface of the wafer using a SiC optical model. The Filmetrics F50 tool was used to evaluate the thickness uniformity across the wafer surface. For stress analysis, the wafer backside was etched using the Oxford 82 system with a CF_4/O_2/Ar gas mixture to expose the front-side curvature. The curvature was then measured using the Flexus tool to calculate intrinsic film stress. Finally, the electrical resistivity of the SiC layers was measured using the Filmetrics R50 system, particularly on the oxide-coated wafers to ensure that the readings were specific to the film itself.
Across both the 800 °C and 850 °C deposition conditions, the silicon carbide thin films demonstrated consistent deposition rates, with no significant fluctuations observed as the gas flow ratio between dichlorosilane (DCS) and acetylene (C_2H_2) was varied. The refractive index of the deposited films remained relatively stable, ranging from 2.7 to 2.9 throughout all runs. In contrast, the resistivity of the films showed a clear downward trend as the DCS-to-acetylene ratio increased, indicating a correlation between gas ratio and film conductivity. Similarly, film stress exhibited a decreasing trend with increasing gas flow ratio at both temperatures. These trends were consistently observed across both sets of wafers and suggest reproducible control of key film properties through process parameter variation. These graphs are shown collectively in Figure 2.
In the doping experiment, ammonia (NH_3) gas was introduced in the deposition process at varying flow rates to explore its effect on the properties of the silicon carbide thin films. Across both 800 °C and 850 °C deposition temperatures, specific NH_3 gas flow settings resulted in films that exhibited high conductivity. At a deposition temperature of 800 °C, a flow rate of 20% max sccm resulted in a film that was highly conductive, as confirmed through resistivity measurements using the Filmetrics R50. Similarly, at 850 °C, a flow rate of 60% max sccm produced a film with high conductivity. These points of interest were repeated to confirm the observed results, and in each case, the outcome remained consistent. However, under these particular doping conditions, the RC Woollam ellipsometer was unable to return a valid model fit or measure the thickness of the films. This in turn resulted in no stress, refractive index, and deposition rate measurements for these wafers. Despite the incomplete optical characterization, the electrical measurements potentially indicate that NH_3 doping successfully altered the electronic properties of the silicon carbide films in certain cases.

Conclusions and Future Steps:

In conclusion this characterization demonstrates that the properties of SiC wafers can be tuned depending on gas ratios, temperatures and even external doping. As the acetylene gas concentration got lower, stress and resistivity also dropped. The introduction of ammonia gas can potentially lead to a more conductive wafer. Future work could focus on specific structural microscopy as the RC Woolam was not able to perfectly characterize some wafers. Other future work could also be in the introduction of ammonia and optimizing the conditions for the best conductivity.

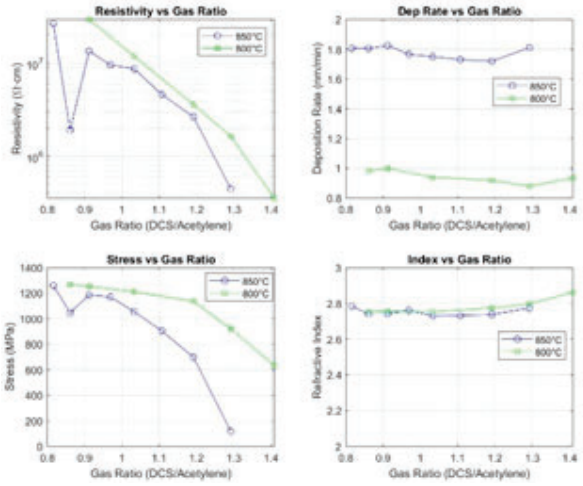

Figure 2: The graphs and their trends are shown above where blue represents 850 °C and green represents 800 °C.

Acknowledgements:

Special thanks to the 2025 Cornell Nanoscale Facility Research Experiences for Undergraduates (CNF REU) Program funded by the National Science Foundation (NSF). I would also like to thank the CNF staff, especially Phil Infante, for their incredible mentorship.

Fabricating Dual-Gated 2D CrSBr Devices to Investigate Nonlinear Transport Effects

CNF Summer Student: Calvin Chiu
Student Affiliation: Physics, The University of Texas at Austin

Summer Program(s): 2025 Cornell NanoScale Facility Research Experience for Undergraduates (CNF REU) Program

Principal Investigator(s): Dan Ralph, Physics, Cornell University

Mentor(s): Bozo Vareskic, Physics, Cornell University

Primary Source(s) of Research Funding: Center for Energy Efficient Magnonics, funded by the U.S. Department of Energy, Office of Science, Basic Energy Sciences under Award #DE-AC02-76SF00515

Contact: dcr14@cornell.edu, bv227@cornell.edu, ckc2398@my.utexas.edu

Summer Program Website(s): https://cnf.cornell.edu/education/reu

Primary CNF Tools Used: Zeiss Supra SEM, Nabity NPGS Nanometer Pattern Generator System, CVC SC4500 Odd-Hour Evaporator, Oxford 81 RIE

Abstract:

The tremendous interest in 2D van der Waals (vdW) materials in condensed matter physics has led to studies on magnetic materials for potential applications in spintronics and quantum information. CrSBr is a magnetic semiconductor that has garnered interest due to its ability to be exfoliated to the 2D limit. However, transport effects in 2D CrSBr such as the nonlinear Hall effect have yet to be explored. In this project, we aim to fabricate functioning dual-gated CrSBr devices and investigate the existence of a nonlinear Hall effect when subjecting the devices to varying parameters.

Summary of Research:

Two-dimensional materials have generated enormous research interest, and the discovery of new materials and ordered phases continues to expand the scope of the field. One category of 2D materials includes van der Waals (vdW) magnets such as chromium sulfur bromide (CrSBr) [1]. CrSBr is particularly interesting from an experimental standpoint, as it is more air-stable compared to other 2D magnetic materials and can be exfoliated relatively easily to the monolayer limit [2].

CrSBr is a magnetic semiconductor exhibiting A-type antiferromagnetic structure; the magnetic moments within a layer are aligned ferromagnetically (same direction) in the plane, while the magnetic moments in adjacent layers are aligned antiferromagnetically (opposite direction). CrSBr also exhibits intriguing electronic and magnetic anisotropies. Due to CrSBr's electronic structure, particularly the orbital composition of its conduction band, electron transport is massively favored along one direction, with the conductivity along the b-axis (σb) being up to 10,000 times larger than σa [2, 3]. Moreover, 2D CrSBr can exhibit strong coupling between its electronic and magnetic structure, including exciton-magnon coupling in twisted bilayer CrSBr [2, 4].

Although various studies have been conducted on CrSBr, there has yet to be definitive measurements regarding a quantum nonlinear Hall effect (NLHE). NLHE is an extension of the classical Hall effect, where a transverse Hall voltage (VH) is induced when a material carrying current is exposed to a perpendicular magnetic field. However, in NHLE, an applied electric field can induce a nonlinear VH, even without introducing a magnetic field. NHLE has been observed and predicted in various materials [5, 6], but we aim to experimentally investigate the NHLE in few-layer CrSBr.

Methods. In this project, we focused on fabricating dual-gated CrSBr transistors for the purposes of investigating whether a nonlinear Hall effect exists, as well as its dependence on temperature, carrier density, and out of plane electric field. To do so, we conducted optimization trials and referenced previous research [5, 7, 8] to develop a working fabrication process, as outlined below:

1. Perform Scotch tape exfoliation onto blank silicon substrates for crystals of few-layer graphene (FLG) and hexagonal boron nitride (hBN). Search for clean ~40 µm x 10 µm FLG and ~50 µm x 50 µm x 70µm hBN flakes.

2. Utilize PDMS viscoelastic stamping to place FLG-hBN on pre-prepared silicon substrates, leaving a segment of FLG exposed for the bottom gate (if convenient).

3. Pattern inner electrodes (e.g. in a double Hall bar geometry) using KLayout and spin-coat substrates with PMMA A4 followed by PMMA A2.

4. Expose/develop samples and deposit 8 nm of platinum using CNF tools, including the Zeiss Supra SEM, Nabity NPGS, and SC4500 Evaporator. Perform lift-off in acetone and tip-based cleaning using an atomic force microscope (Fig. 1).

5. In an oxygen- and water-free glove box, exfoliate and search for ~10 µm x 5 µm few-layer CrSBr and more hBN flakes. Stamp CrSBr flakes such that the flake contacts all inner electrodes, and stamp hBN to cover all but the exposed FLG.

6. Pattern openings to the inner electrodes. Spin-coat and expose/develop. Etch the exposed segments to remove the hBN using Oxford 81 RIF.

7. Pattern outer electrodes, a top gate, and bottom gate(s) to connect to the pre-prepared bonding pads. Spin-coat, expose/

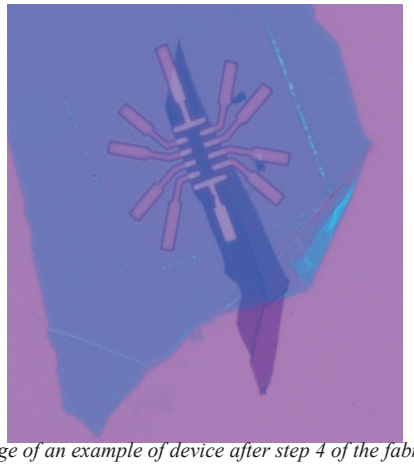

Figure 1: Image of an example of device after step 4 of the fabrication process.

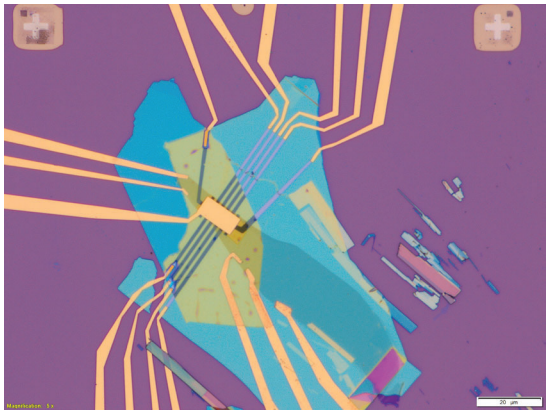

Figure 2: Image of an example device after the full fabrication process.

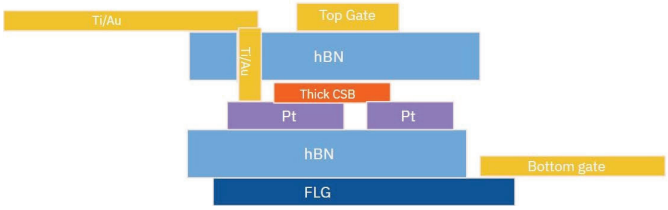

Figure 3: Transverse view of the device "stack", with colors corresponding to Figure 2.

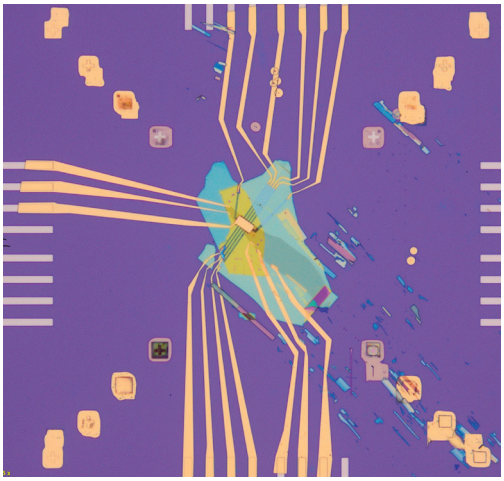

Figure 4: Zoomed-out image of Figure 2.

develop, deposit 10nm Ti/90 nm Au, and perform lift-off (Fig. 2-4).

Conclusions and Future Steps:

Through extensive testing and trial-and-error, we have established a working fabrication process for creating dual-gated 2D CrSBr devices. Despite the supposed air stability of CrSBr, the exfoliation in the glove box and complete insulation by the top hBN were required to prevent the CrSBr from degrading and losing electrical contact after several hours. Our fabrication process may also apply to other air-sensitive 2D materials with transport properties of interest.

With our obtained measurements, we aim to extract the conductivity tensors of few-layer CrSBr in the near future. Further studies can be conducted to verify the obtained results improve the fabrication efficiency.

Acknowledgements:

Many thanks to the 2024 Cornell NanoScale Facility Research Experiences for Undergraduates (CNF REU) Program funded by the National Science Foundation under Grant No. NNCI-2025233, and the National Nanotechnology Coordinated Infrastructure. Special thanks to Prof. Dan Ralph and Bozo Vareskic for all of their guidance and support.

References:

[1] Burch, K. S. et al. https://doi.org/10.1038/s41586-018-0631-z
[2] Michael E. Ziebel et al. DOI: 10.1021/acs.nanolett.4c00624
[3] Wu, F. et al. DOI: 10.1002/adma.202109759
[4] Sun, Y. et al. DOI: 10.48550/arXiv.2506.10080
[5] Chichinadze, D. V. et al. DOI: 10.48550/arXiv.2411.11156
[6] Min L et al. DOI: 10.1038/s41467-023-35989-0
[7] Sun, S. et al. DOI: 10.48550/arXiv.2507.15853
[8] Bhatia, P. et al. DOI: 10.1016/S0968-4328(24)00164-1

Baseline Etch Processes: Evaluating Etching and Stripping Tools

CNF Summer Student: Scott Coonrod
Student Affiliation: Cornell University College of Engineering

Summer Program(s): 2025 Cornell NanoScale Facility Research Experience for Undergraduates (CNF REU) Program
Mentor(s): Aaron Windsor, Cornell NanoScale Science and Technology Facility, Cornell University
Primary Source(s) of Research Funding: National Science Foundation under Grant No. NNCI-2025233,
Contact: windsor@cnf.cornell.edu, src252@cornell.edu
Summer Program Website(s): https://cnf.cornell.edu/education/reu
Primary CNF Tools Used: Oxford 81, Oxford 82, PT740, FilMetrics F50, P-7 Profilometer

Abstract:

Reactive Ion Etching is a technique that can achieve highly anisotropic etches, as well as high selectivity. Etching is performed by high energy ions as well as reactive species that interact with the surface, with an etch rate dependent on the recipe and the material being etched. Certain tools in the cleanroom, such as the PT740, Oxford 81, Oxford 82, and Glen 1000 all have stated etch rates for certain recipes. However, over time, these rates have changed from when the measurements were originally taken, meaning the manuals may no longer be accurate. The goal of this project is to measure the current etch rates of these machines across many recipes and materials to update the manuals, ensuring that future users will be able to more precisely etch their samples.

Summary of Research:

When measuring etch rates on the PT740, Oxford 81, and Oxford 82 tools, recipes stated in their respective manuals were used. Measurements of the samples before and after etching were performed by the FilMetrics F50 optical metrology tool, allowing for the characterization of etch rates across the sample. Silicon oxide wafers were deposited using 4 different PECVD methods; high rate, low rate, HDP, and TEOS deposition. Silicon Nitride wafers (figure 1) were produced with PECVD, LPCVD, HDP-CVD, as well as with the NIT N=2 recipe on the PT Takachi HDP-CVD. Carbide wafers were made by LPCVD. All aforementioned wafers were produced by Aaron Windsor. The Glen 1000 oxygen plasma tool was also characterized alongside the RIE machines. Three different resists were measured: Shipley 1813, nLof Az 2020, and SPR220-3.0. These were characterized using the RIE configuration of the Glen 1000 (figure 4), with etch rates measured using the P-7 profilometer. The final characterization that was performed was BARC (Bottom Anti-Reflective Coating) strip times. With a

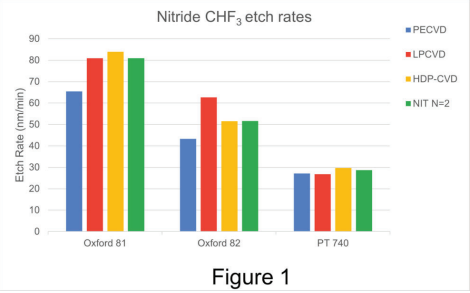

Figure 1: Etch rates over 3 tools and 4 deposition methods of silicon nitride, showing trend that the Oxford 81 is the fastest, followed by the Oxford 82, then the PT740.

ARC removal tool:	Wattage	Minutes:
Glen rack A	500W	5
Glen rack B	500W	1
Glen rack C	500W	4
Glen rack A	400W	5
Glen rack B	400W	1
Glen rack C	400W	6
Anatech	300W	3
Yes asher	100W	14
Yes ecoclean asher	3000W	1

Figure 2

Figure 2: Time to remove ARC layer over different tools.

thin layer of BARC, incremental 1-minute runs on different machines were performed, until the coating was no longer measurable on the wafer. Two machines were able to remove the layer in under a minute; the Glen 1000 rack B (either 400 or 500 W), as well as the YES Ecoclean Asher using the recipe "0resist_strip_1min" (figure 2).

Etch/strip rates:

When comparing the measured etch rates with the etch rates stated in the manuals, two machines have changed considerably since the last time they were characterized.

The Oxford 82 recipe "CHF_3 / O_2 oxide etch" was stated to have an etch rate of 43 nm/min, however, the measured etch rate is only around 25 nm/min. The "CF_4 / O_2 oxide etch" also has decreased over time, as the stated etch rate is 42 nm/min, while the measured etch rate is

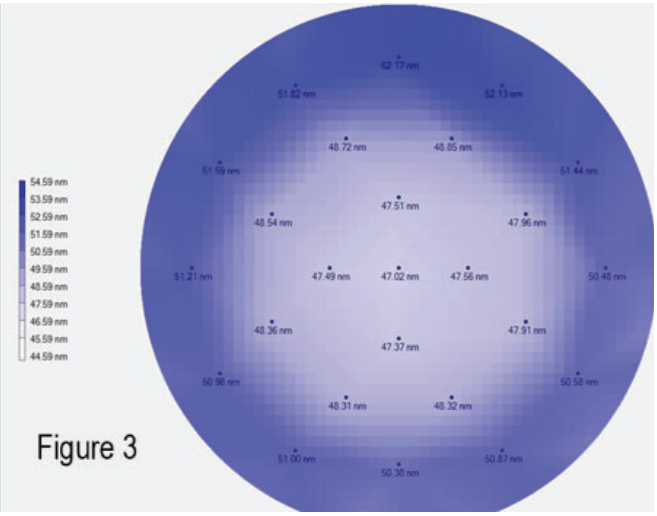

Figure 3: Difference map of before and after an etch with the PT740, showing a higher etch rate along the edge of the wafer.

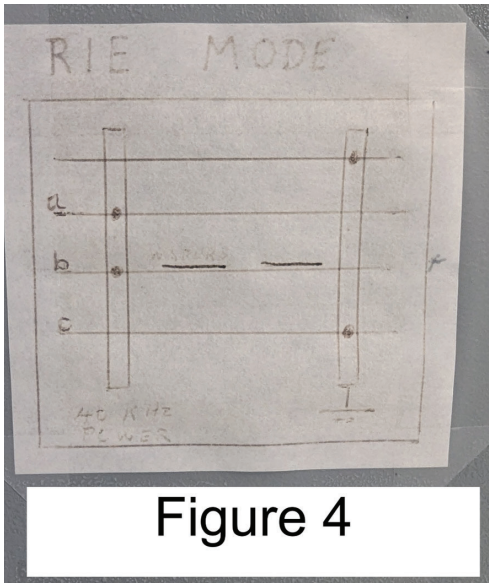

Figure 4: Design showing the configuration of the Glen 1000 during testing, with 1st and 4th rack being grounded, and the 2nd and 3rd rack attached to power.

closer to 21 nm/min. The Glen 1000, has significantly changed since the last characterization, which was taken around 2003. The old stated values for racks A, B, and C are respectively; 300nm/10min, 730nm/10 min, and 280nm/10 min. The current measured values are 92 nm/10 min, 410 nm/10 min, and 41 nm/10 min. The PT740 manual had one stated recipe that did not match the measured rate, that being the 'CHF_3 / O_2 nitride etch LSN", with the stated value being 19 nm/min, and the measured value 27 nm/min. However, this etch rate was characterized recently, and it is suspected that the etch rates of the PT740 vary due to other uncontrolled factors, so further testing would be required to definitively state whether this recipe needs to be updated.

Uniformity:

Tests were run on the RIE machines using 100mm wafers. The two Oxford 80 tools have similarly uniform etches, with a uniformity of around ± 2.5-3%. The Oxford 81 appears to etch slightly faster in the center than the outside, with the Oxford 82 being the opposite. With the PT740, however, it is clearly visible that the outside of the wafer etches with the highest rate, with the outside of the wafer (10mm from the edge) etching around 10% faster than the middle (figure 3). This machine has a uniformity across the wafer of around ± 5%.

Conclusions and Future Steps:

When etching Silicon compounds, the tool with the highest etch rate is the Oxford 81, followed by the Oxford 82 then the PT740. The fact that the two Oxford tools have differing etch rates is surprising, given that they are two identical instruments. The reason for this discrepancy is unclear, and determining and correcting the cause of this difference is a possible area for future work. Using this new data the recipes for the Oxford 82 stated in this report should be updated, as well as all the numbers on the Glen 1000. BARC stripping can now be suggested for some users with material restrictions to be done in the Glen 1000 rack B or the YES Ecoclean Asher could be used.

Acknowledgements:

Special thanks to Aaron Windsor and Lynn Rathbun for enabling me to have this amazing hands-on experience, as well as providing consistent support throughout this summer. I also would like to thank the rest of the Cornell NanoScale Science and Technology Facility for allowing me to perform this research.

References:

[1] Coburn, J.W., and Harold F. Winters. "Plasma etching—A discussion of mechanisms." Journal of Vacuum Science and Technology, vol. 16, no. 2, 1979. Accessed 4 8 2025.

[2] Link to data spreadsheet containing all measured etch rates: https://1drv.ms/x/c/402b9da0fc160dae/Efrv37R3g3JJlw8Ylu3WqJoBCddXBHjEDM6YexCmTonH5w?e=1vMcMx

Fabrication of Manhattan-style Josephson Junctions

CNF Summer Student: Gabriele Di Gianluca
Student Affiliation: Physics, University of Florida

Summer Program(s): 2025 Cornell NanoScale Facility Research Experience for Undergraduates (CNF REU) Program
Principal Investigator(s): Valla Fatemi
Mentor(s): Simon Reinhardt, Maciej Olszewski, Lingda Kong
Primary Source(s) of Research Funding: NORDTECH (SQ Fab)
Contact: vf82@cornell.edu, digianlucag@ufl.edu
Summer Program Website(s): https://cnf.cornell.edu/education/reu
Research Group Website: https://fatemilab.aep.cornell.edu/
Primary CNF Tools Used: Angstrom-Q, JEOL 6300 E-beam Lithography System, Zeiss Ultra SEM, GCA AS200 i-line Stepper, Heidelberg DWL2000, AJA Sputter 1

Abstract:

Qubits based on superconducting quantum circuits are one of the most promising platforms for quantum computing [1]. The critical component of these superconducting qubits is the Josephson Junction. We use a Josephson Junction which is a superconductor-insulator-superconductor interface that relies on the tunneling of Cooper pairs through the thin insulating barrier [1]. Once below the critical temperature of the superconducting material, the Josephson Junction can now conduct a current without any applied voltage, exhibiting the Josephson Effect. This nonlinear current creates the key anharmonicity needed to create a qubit [2]. In this research, we fabricate Manhattan-style Josephson Junctions in the Angstrom-Q and characterize the oxidation process.

Summary of Research:

The main two types of Josephson Junctions are Dolan and Manhattan-style. Dolan-style junctions rely on a shadow evaporation method where Electron-Beam lithography on the JEOL 6300 is performed onto a PMMA/MMA resist stack. During this lithography, a bridge is defined, and two evaporations are performed at different angles with an oxidation in between. This overlap between the two evaporation defines our junction area, a key factor in determining the properties of the Josephson Junction. The main downside to this style is that the bridge used is fragile and can frequently collapse, therefore halting the fabrication process. Additionally, the bridge can vary between lithography runs due to resist thickness. This inconsistency in the bridge leads to an inconsistency in junction area, which changes the parameters of the qubit. In an effort to increase reproducibility in our qubit fabrication, we began to fabricate Manhattan-style Josephson Junctions using the new Angstrom-Quantum evaporator, designed specifically for this purpose. Manhattan-style junctions (Figure 1) are a bridge-less technique that use a similar PMMA/MMA resist stack, but instead rely on an evaporation into two different trenches [3]. As opposed to Dolan-style junctions, in this case, the area of our junctions is only determined by the lithography. This, coupled with the fact that there is no

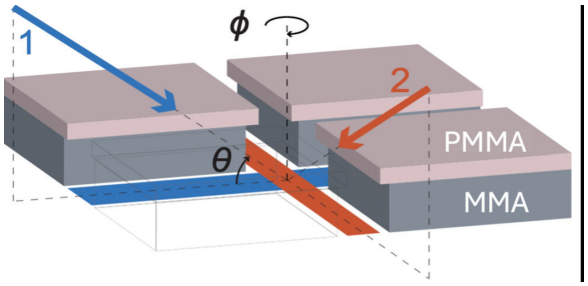

Figure 1:

bridge involved, increases our reproducibility between fabrication runs.

The main reason we care about the area of our junction is that it affects critical current, I_c, the maximum current the junction can hold before returning to a non-zero resistance state. The critical current is given by the Ambegaokar–Baratoff relation (Figure 2a), in which the superconducting gap of Aluminum is known and the normal state resistance, R_n, can be obtained by a room temperature two-probe resistance measurement. From the critical current, we can then determine the Josephson Energy, E_J (Figure 2b). E_J is a key term in the Hamiltonian of our circuit and determines the circuit dynamics, primarily our qubit frequency, a critical

a)

$$I_c = \frac{\pi\Delta}{2eR_n}$$

Δ = Superconducting gap
R_n = Normal state resistance

b)

$$E_J = \frac{\Phi_0}{2\pi} I_c \propto I_c$$

Magnetic flux quantum: $\Phi_0 = \frac{h}{2e}$ =constant

Figure 2:

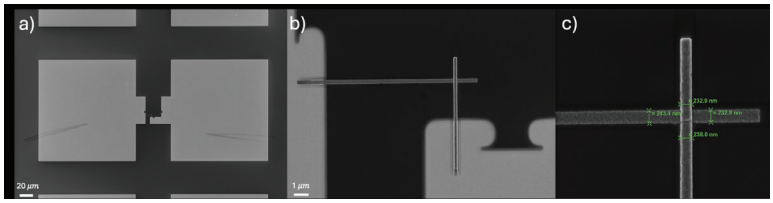

Figure 3:

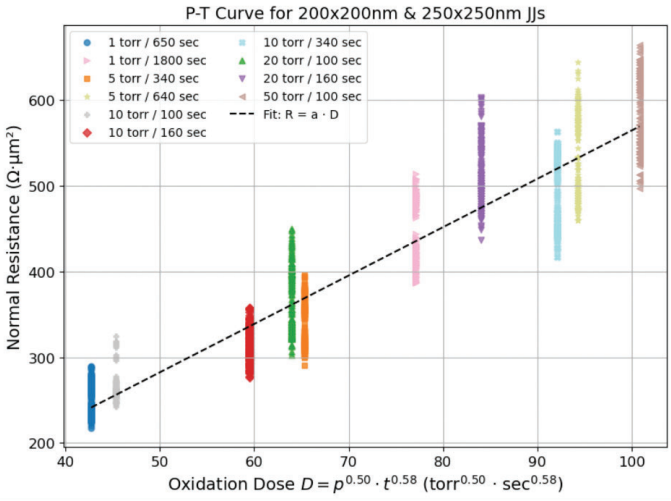

Figure 4:

number in benchmarking qubit performance [1].

Our fabrication process began by doing a standard HF clean of our 100mm Si wafer in order to remove the native oxide layer. Then we spun on a LOR 3A and S1813 photoresist stack before patterning bonds pads using the i-line stepper on a mask written in the Heidelberg DWL2000. After developing on a Hamatech automatic developer, we deposited Ti-seeded Pt using the AJA 1 Sputter tool. The 5nm of Ti acts as an adhesion layer for the 80nm of Pt which does not naturally oxidize, making it compatible with our probe station. After doing lift-off in Remover PG overnight, we spun on a PMMA/MMA e-beam resist stack. This allowed us to pattern our Josephson Junctions in the JEOL 6300 Electron-Beam Lithography system. Onto our wafer, we patterned 100 200x200nm and 100 250x250nm junctions. Before depositing, we cleaved our wafer into chips and developed them in IPA:DI (3:1) for 2 minutes. Once loaded into the Angstrom-Q, we do an in-situ argon milling to remove any unwanted oxide that could prevent poor contact. We then deposit 20nm of Al for our bottom electrode at a rate of 2 A/s and a chamber pressure <5e-8. Our oxidation step varies with pressures from 1 to 50 torr and 1 to 30 minutes. Our top electrode is 70nm of Al and is deposited at a similar chamber pressure as the bottom electrode. Before taking our sample out, we do a post-oxidation step instead of letting the sample oxidize arbitrarily in atmosphere. Then we do lift-off in heated DMSO at 80-90 C overnight. Finally, we measure room temperature resistance using a Keithley SourceMeter and a probe station with Tungsten tips. After probing resistance, SEM images were taken on the Zeiss Ultra SEM in order to calculate the area of our junctions and evaluate the success of lift-off (Figure 3).

We iterated on our fabrication many times in order to produce 20 data points across JJs with a 20nm bottom electrode. With this data, we plotted the normal resistance, resistance of our junctions times the area, versus the oxidation dose, a combination of the pressure and time of the oxidation. The value of the exponents assigned to pressure and time and the linear fit to our data was optimized (Figure 4). We observe our data aligns with our linear fit and with previous work [4]. We also compute the variability of junction resistance across a die and observe a variance <5%, which is acceptable for qubit devices.

Conclusions and Future Steps:

We successfully demonstrated the fabrication of Manhattan-style Josephson Junctions in the Angstrom-Q. We also characterized and optimized the fabrication process by constructing a pressure-time curve. This curve will allow us to determine the oxidation dose necessary to obtain a junction of a desired resistance with minimal trial and error.

The next step will be move away from Dolan-style junctions and incorporate Manhattan-style Josephson Junctions into our qubit fabrication process. As we do multiple fabrication runs, we will see whether the junction properties are reproducible and whether Manhattan junctions have any advantage over Dolan junctions. Another possibility will be to do an aging study of Josephson Junctions. This would involve measuring the resistance of junctions over at least a month and observing how the resistance changes over time.

References:

[1] Rasmussen et al., "Superconducting Circuit Companion---an Introduction with Worked Examples."

[2] Krantz et al., "A Quantum Engineer's Guide to Superconducting Qubits."

[3] Kreikebaum et al., "Improving Wafer-Scale Josephson Junction Resistance Variation in Superconducting Quantum Coherent Circuits."

[4] Zeng et al., "Direct Observation of the Thickness Distribution of Ultra Thin AlOx Barriers in Al/AlOx/Al Josephson Junctions."

Domain Switching in Twisted Double Bilayer Graphene

CNF Summer Student: Peter Golemis
Student Affiliation: Physics and Electrical & Computer Engineering, University of Illinois Urbana-Champaign

Summer Program(s): 2025 Cornell NanoScale Facility Research Experience for Undergraduates (CNF REU) Program
Principal Investigator(s): Kenji Yasuda
Mentor(s): Daniel Brandon
Primary Source(s) of Research Funding: National Science Foundation under Grant No. NNCI-2025233)
Contact: kenji.yasuda@cornell.edu, db923@cornell.edu, golemis3@illinois.edu
Summer Program Website(s): https://cnf.cornell.edu/education/reu
Research Group Website: https://www.yasudalab.org/home
Primary CNF Tools Used: Oxford 81 RIE, SC4500 Odd-Hour Evaporator, Zeiss Supra SEM, Nabity Nanometer Pattern Generator System

Abstract:

For over two decades, the properties of two-dimensional (2D) graphene films have been rigorously explored, exhibiting a variety of profound electronic phenomena [1]. Few-layer graphene has received great attention due to the wide range of electronic band structures realized across its various stacking orders [2]. Different coexisting stacking orders are obtained by precisely controlling the twist angle between two bilayer graphene flakes, generating Bernal (ABAB) and rhombohedral (ABCA) domains. In this work, we obtain transport measurements of small-angle twisted double bilayer graphene (TDBG) Hall bar devices with this domain structure, which exhibit gate-tunable domain switching. This platform enables the observation of the interplay between domain switching and the electronic properties of Bernal and rhombohedral graphene.

Summary of Research:

Device Fabrication:

Bernal (Fig. 1a) and rhombohedral (Fig. 1b) ordered graphene are two possible stacking configurations of four-layered graphene systems. Introducing a small twist angle between two bilayer graphene films enables the formation of large coexisting Bernal and rhombohedral domains. The electronic properties of small-angle TDBG are probed in double-gated stacks (Fig. 1c) constructed using a PDMS/PC dry transfer process. High- quality uniform gates consisting of a thin hexagonal boron nitride (hBN) dielectric and conducting graphite flake are used to tune the carrier density and out-of-plane displacement field through the TDBG. Initially, the bottom gate is stacked and placed onto a pre-patterned Si/SiO2 substrate (Fig. 1d). Mechanically exfoliated bilayer graphene flakes are then identified using optical microscopy and cut into two pieces by applying a high-frequency alternating voltage to a conductive atomic force microscope (AFM) tip [3].

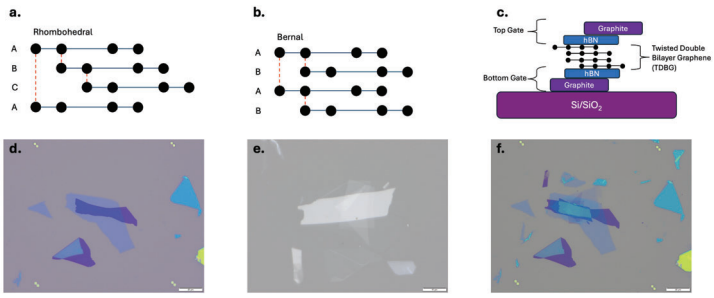

Figure 1: a,b, Visualization of rhombohedral and Bernal stacking orders in TDBG. c, Profile schematic of a double gated TDBG stack. d, Bottom gate placed on a pre-patterned chip. e, Complete top stack on PDMS/PC stamp. f, Complete stack consisting of a bottom gate (Fig. 1d) and top stack (Fig. 1e).

Scanning the conductive AFM tip over a graphene flake in a humid environment drives an anodic oxidation process to selectively remove regions of the flake with minimal induced strain on the crystal lattice. Implementing the dry transfer process, a top gate is fabricated separately by stacking graphite on top of a thin hBN flake. The first half of the bilayer graphene flake is stacked beneath the top gate, and the other half is rotated by $\theta = 0.03°$. Finally, the rotated graphene is stacked beneath the graphene on the top gate (Fig. 1e), which is then released onto the bottom gate on the pre-patterned chip (Fig. 1f).

After stacking the double-gated TDBG structure, a Hall bar etching mask with 1D graphene contacts is designed on a clean region of the device. The device is coated with PMMA 950K

A4 resist, and the etching mask is written using e-beam

lithography. Exposed graphite and hBN regions are etched completely using low-power O_2 and CHF_3/O_2 plasma, respectively. After the Hall bar geometry has been defined (Fig. 2a), the device is coated with PMMA 495K A4 and PMMA 950K A2 to write the electrode pattern connecting to the TDBG contacts. After writing the pattern using electron beam lithography, the exposed contact regions of the Hall bar are then etched completely to expose a 1D TDBG contact region.

Finally, chromium, palladium, and gold contacts are deposited onto the chip, and the remaining resist is removed in an acetone bath (Fig. 2b).

Results:

Sweeping the top and bottom gate voltages of the device at T = 1.5K gave rise to gate- dependent signatures in the hole-doped region (Fig. 3a). This implies a gate-induced change in the structure being measured, in which graphene layers slide between a Bernal and rhombohedral stack ordering. By applying an external magnetic field, the magnitude of the switching response varies dramatically from the B = 0T case. After applying an external field B = 2T, the switching response in the higher hole density region is emphasized, whereas the switching response closer to charge neutrality is emphasized in the zero-field case (Fig. 3a,c). Having defined part of the switching region, the measurement scheme demonstrated in Fig. 3b is conducted, in which the device switches deep into the rhombohedral phase. From the rhombohedral-dominated phase, two measurements of the switching response Rxx(n, D) are made by ramping Vtg (Vbg) and then sweeping Vbg (Vtg) to map out the entire switching region. The sum of these plots highlights multiple boundaries in the hole-doped region (Fig. 3d). These distinct equipotential lines correspond to the free energy required to overcome the domain wall pinning energy to switch from one order to another.

Conclusions and Future Steps:

These results demonstrate the transport behaviors of domain switching in multi-layer 2D materials. Domain switching can be used to gain new insights into exotic transport phenomena. Future experiments may involve domain switching in platforms with different stacking configurations, twist angles, and crystals. It would also be of great interest to explore emergent transport properties unique to these different stacking orders and their interactions in a domain switching platform.

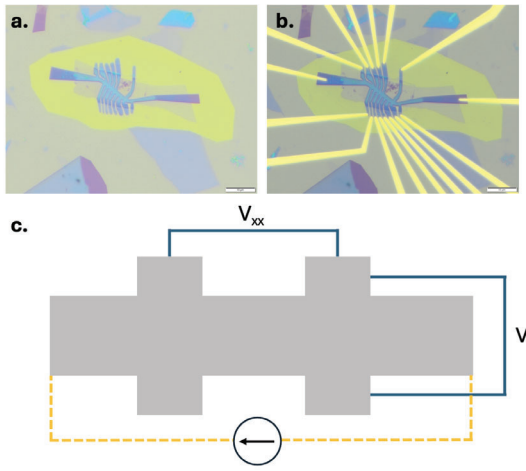

Figure 2: a, Complete stack (Fig. 1f) etched into a Hall bar geometry. b, Cr/Pd/Au contacts deposited on 1D TDBG contacts. c, Hall bar measurement configuration.

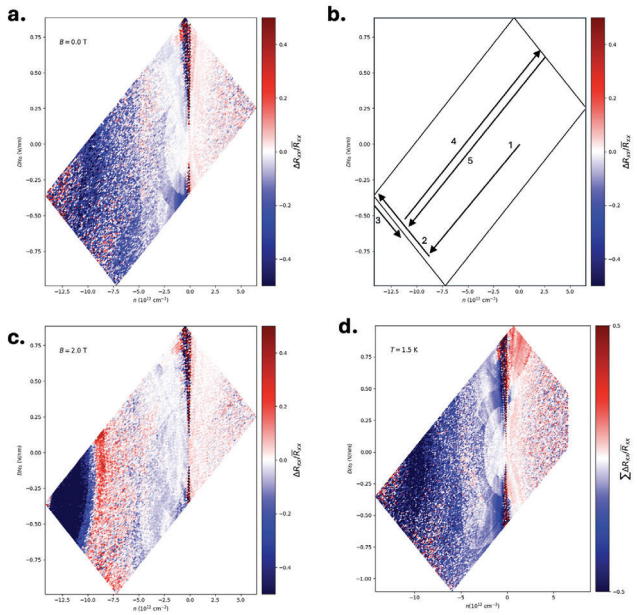

Figure 3: a, Switching boundary between Bernal and rhombohedral phases. This is defined by the mean normalized difference between the forward and backward bottom gate sweeps. b, Measurement scheme to define switching boundary in Fig. 3a. c, Same measurement as Fig. 3a under B = 2T. d, Sum of the mean normalized differences from the bottom and top gate sweeps. This plot maps the entire rhombohedral-Bernal switching region.

References:

[1] K. S. Novoselov et al., Electric Field Effect in Atomically Thin Carbon Films.Science306,666-669(2004). https://doi.org/10.1126/science.1102896

[2] Lui, C., Li, Z., Mak, K. et al. Observation of an electrically tunable band gap in trilayer graphene. Nature Phys 7, 944–947 (2011). https://doi.org/10.1038/nphys2102

[3] Electrode-Free Anodic Oxidation Nanolithography of Low-Dimensional Materials Li, H. et al. Nano Letters 2018 18 (12), 8011-8015 DOI: 10.1021/acs.nanolett.8b04166

Determining Out-of-Plane Structure via Electron Diffraction

CNF Summer Student: Tyler Hendee
Student Affiliation: Department of Engineering Physics, University of Wisconsin Platteville

Summer Program(s): 2025 Cornell NanoScale Facility Research Experience for Undergraduates (CNF REU) Program
Principal Investigator(s): Judy Cha, Department of Materials Science & Engineering, Cornell University
Mentor(s): Stephen Funni, Natalie Williams
Primary Source(s) of Research Funding: National Science Foundation under Grant No. NNCI-2025233
Contact: rjc476@cornell.edu, hendeet@uwpatt.edu, sdf68@cornell.edu, nlw49@cornell.edu
Summer Program Website(s): https://cnf.cornell.edu/education/reu
Research Group Website: https://cha.mse.cornell.edu/

Abstract:

In situ studies of phase transitions in materials are essential to understanding structure evolution, and thus engineering for novel or advanced applications [1]. This is especially true in battery materials where dramatic, intercalation-induced phase transitions impact safety, reliability, and performance [2]. Scanning transmission electron microscopy (S/TEM) provides simultaneous imaging, diffraction, and spectroscopy data from a single instrument. However, in situ intercalation experiments in the TEM are uncommon and often rely on highly specialized holders [3]. Here we characterize the complete lithiation-induced phase transition in the layered van der Waals (vdW) material, lanthanum tritelluride ($LaTe_3$), using a standard electrical biasing holder by fabricating electrochemical cells that are liquid-free.

Throughout lithiation of the $LaTe_3$ flake, we observed at least two distinct phase transformations, various $LaTe_3$ stackings, and an expansion and subsequent relaxation of the in-plane lattice. During this experiment, several types of data were acquired: atomic resolution and low-magnification STEM imaging, electron energy loss spectroscopy (EELS), and spatially resolved diffraction using four-dimensional STEM (4D STEM). The combined analysis of these datasets reveals the morphological, electronic, chemical and structural changes of the flake during intercalation. The experimental patterns observed were replicated by multislice simulations (abTEM [5]) from different 1x1x3 supercells with lithium ordering in vdW gap interstitials (Figure 2).

A later experiment includes 4D STEM data from convergent beam electron diffraction (CBED). This provides out-of-plane structure due to interactions with the higher order Laue zone (HOLZ) of the reciprocal lattice. Simulations confirm individual stackings are distinguishable from each other and from out-of-plane disorder. CBED analysis via Hough circle transforms [6] allows us to measure out-of-plane strain.

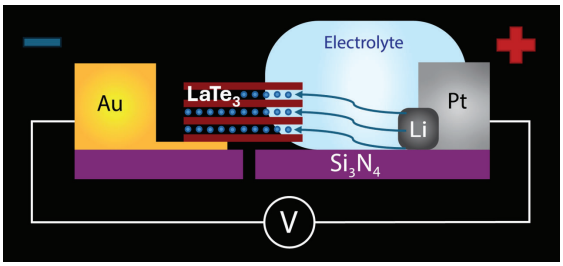

Figure 1: The all solid-state electrochemical cell, where the voltage bias controls lithium intercalation in the vdW gaps between $LaTe_3$ layers.

Summary of Research:

In each in situ experiment, we utilize an off-the-shelf electronic chip (e-chip) placed in a standard Protochips Fusion350 heating/biasing holder. The all solid-state electrochemical cell is displayed in Figure 1. At the start of the experiments, the $LaTe_3$ flake is in the pristine state, as shown in Figure 2a. EELS analysis tells us there is no detectable lithium in this phase. In the first experiment, after measuring an open circuit voltage of 2.3 V, we initiated intercalation by lowering the cathode potential to 0 V (vs Li anode). After 10 minutes, we observed an intercalation-induced new phase propagated across the flake, verified by low magnification STEM imaging. The EELS data taken 35 minutes after initiating intercalation showed an increase in intensity following the Li-K edge onset at 57 eV. Representative diffraction patterns in this phase revealed two lithiated structures with the same ordering: one maintaining the bulk stacking and one with a layer shifted by half the lattice (Figure 2b), as seen in the alignment of Te-nets across the vdW gap. 4D STEM analysis at this stage showed significant in-plane lattice expansion of approximately 1.5%.

After continuing intercalation at the 0 V cathode potential, the flake did not exhibit further significant changes. Approximately 4 hours into the experiment, we lowered the cell voltage to -9 V. By the 5.5-hour mark, we observed a second major phase transformation. The lithium-ordering superlattice disappeared (Figure 2c) and the previous in-plane lattice expansion had relaxed. Simulated diffraction of the proposed structures matches the experimental diffraction patterns from their respective lithiated phases (Figure 2). We attribute the in-plane strain relaxation to the addition of out-of-plane unit cell expansion. CBED simulations result in diffraction patterns containing HOLZ rings, whose radii we measure with Hough circle transforms. This analysis is robust to sample tilt, and the measured radius of HOLZ rings is inversely correlated with the out-of-plane strain of each stacking (Figure 3). The CBED patterns of different stackings are distinguishable from one another, which allows us to measure out-of-plane strain while preserving phase information.

We determined the optimal TEM parameters with more simulations, then ran the experiment again using scanning CBED. Preliminary analysis shows significant out-of-plane disorder in later stages of lithiation. This causes the HOLZ rings to blur, making them more challenging to measure with the Hough circle transform alone. We aim to increase the precision of our measurement method and subsequently pair it with a radial average integration technique. Currently, we are using simulations to investigate the resultant diffraction patterns caused by various types of disorder.

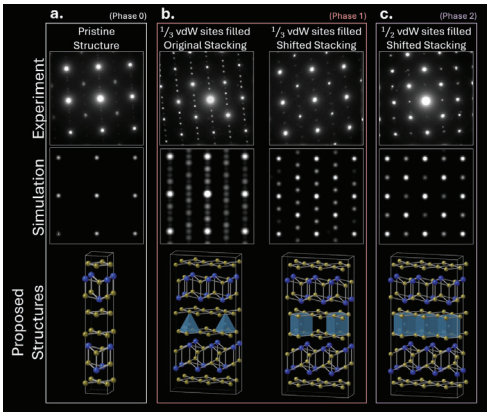

Figure 2: (a) The pristine structure, which contains no lithium, (b) the first phase transformation, where 1/3 of the vdW sites are filled and we observe the original as well as a shifted stacking, and (c) the second phase transformation, where 1/2 of the vdW sites are filled and we only observe shifted stacking.

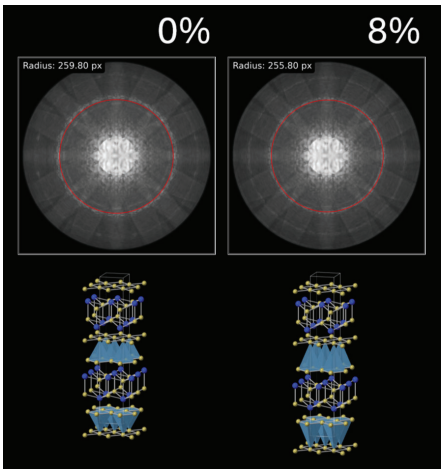

Figure 3: A demonstration of the inverse relationship between out-of-plane unit cell expansion and HOLZ ring radius.

Conclusions and Future Steps:

In situ experiments allowed us to identify two distinct phase transformations of $LaTe_3$ via multimodal STEM (imaging, EELS, and 4D STEM). To enable this complete characterization in a single experiment, we developed an all solid-state electrochemical cell on a standard Si_3N_4 membrane-style TEM e-chip. We developed techniques for mapping structural information during the intercalation process, including out-of-plane stacking and unit cell expansion. We perform these measurements over large fields of view using 4D STEM. With abTEM multislice simulations, we determined optimal CBED parameters and repeated the intercalation experiment. Looking forward, we aim to improve measurement precision, further investigate out-of-plane disorder, and complete the remaining analysis of our latest dataset. Our method should enable future investigations of other intercalation materials to directly and comprehensively observe their phase transformations.

References:

[1] M. Wang, S. Xu, and J. J. Cha, "Revisiting Intercalation-Induced Phase Transitions in 2D Group VI Transition Metal Dichalcogenides," Advanced Energy and Sustainability Research, vol. 2, no. 8, p. 2100027, 2021, doi: 10.1002/aesr.202100027.

[2] M. Rajapakse et al., "Intercalation as a versatile tool for fabrication, property tuning, and phase transitions in 2D materials," npj 2D Mater Appl, vol. 5, no. 1, pp. 1–21, Mar. 2021, doi: 10.1038/s41699-021-00211-6.

[3] C. Wang, R. Zhang, J. Li, and H. L. Xin, "Resolving electrochemically triggered topological defect dynamics and structural degradation in layered oxides," Proceedings of the National Academy of Sciences, vol. 122, no. 3, p. e2409494122, Jan. 2025, doi: 10.1073/pnas.2409494122.

[4] M. W. Tate et al., "High Dynamic Range Pixel Array Detector for Scanning Transmission Electron Microscopy," Microscopy and Microanalysis, vol. 22, no. 1, pp. 237–249, Feb. 2016, doi: 10.1017/S1431927615015664.

[5] J. Madsen and T. Susi, "The abTEM code: transmission electron microscopy from first principles," Open Research Europe, vol. 1, p. 24, Mar. 2021, doi: 10.12688/openreseurope.13015.1.

[6] Xie, Yonghong, and Qiang Ji. "A new efficient ellipse detection method." Pattern Recognition, 2002. Proceedings. 16th International Conference on. Vol. 2. IEEE, 2002, doi: 10.1109/ICPR.2002.1048464

Silicon Interposer for Millimeter-Wave Heterogenous Integration: Doped vs. High Resistivity Substrates

CNF Summer Student: Kenta Lin
Student Affiliation: Ming Hsieh Department of Electrical and Computer Engineering; University of Southern California

Summer Program(s): 2025 Cornell NanoScale Facility Research Experience for Undergraduates (CNF REU) Program
Principal Investigator(s): James C. M. Hwang
Mentor(s): Jin Hong Joo
Primary Source(s) of Research Funding: National Science Foundation under Grant No. NNCI-2025233, SUPREME
Contact: jch263@cornell.edu, kentalin@usc.edu, jj593@cornell.edu
Summer Program Website(s): https://cnf.cornell.edu/education/reu
Research Group Website: https://cha.mse.cornell.edu/
Primary CNF Tools Used: SUSS MA6-BA6 Contact Aligner, AJA Sputter Deposition, UNAXIS 770 Deep Silicon Etcher, PlasmaTherm Versaline System, Veeco Savannah ALD, ReynoldsTech Cu ECD Hood, DC Probe Station, Microwave Small-Signal Probe Station

Abstract:

As the demand for heterogeneous-integrated RF chips increases, interposers for millimeter-wave circuits using through-silicon vias (TSVs) have become increasingly important due to their low loss and high- power capacity across a wide frequency range. For frequencies above 110 GHz, substrate-integrated waveguides (SIWs) are small enough to be integrated in Si interposers for high-power interconnects.

They can also be used to form high-quality passive devices such as filters and antennas, which have been difficult to integrate on-chip. This enables system-on-chip. In this study, we investigate the fabrication of SIWs and grounded coplanar waveguides (GCPWs) in silicon (Si) interposers with a thickness on the order of 200 um with resistivities ranging from 10 to 1 kΩ·cm. Thin Si wafers were patterned and etched using the Bosch deep reactive ion etching (DRIE) process to create TSVs. The TSVs are then metallized with platinum (Pt) using atomic layer deposition (ALD) and filled with copper (Cu) using electroplating deposition. DC measurements confirm a TSV series resistance of less than 1 Ω. Small-signal millimeter- wave on-wafer measurements show that the coplanar interconnects fabricated on high-resistivity (HR, resistivity > 1 kΩ·cm) Si have an insertion loss of 0.7 dB/mm at 40 GHz, an order of magnitude better

than the same coplanar interconnects fabricated on doped Si (resistivity < 10 Ω·cm).

Summary of Research:

Si is the most extensively used material in semiconductor devices due to its exceptional electrical and mechanical properties, including a high dielectric constant, electrical resistivity, breakdown strength, and low loss tangent. These characteristics make it an attractive candidate for SIWs. However, its relatively low mechanical toughness and high thermal conductivity compared to materials like silicon carbide (SiC) pose challenges during processing, particularly in etching processes. Our group has previously demonstrated SiC as a viable substrate material for SIW processing. The methodology developed for SiC SIW fabrication is adapted as a proof of principle for Si SIW fabrication.

To develop a processing recipe for Si-based SIWs, we used a thinned HR Si wafer with a thickness of approximately 200 μm and resistivity greater than 1 kΩ·cm. Building on a similar methodology used for SiC SIWs while leveraging the more mature and faster etching processes available for Si, we began by depositing a 50 nm layer of aluminum oxide (Al2O3) on the wafer's backside using AJA Sputter

Deposition. Al2O3 was selected as the etch mask due to its excellent masking performance in the Bosch DRIE process for Si, providing a high selectivity greater than 1:1000.

The DRIE was performed using either the UNAXIS 770 Deep Silicon Etcher or the PlasmaTherm Versaline System. To ensure effective cooling during etching, the Si wafer was bonded to a sapphire carrier wafer using cool grease. The etching chemistry employed C4F8/SF6, which react with Si to

anisotropically form vias. As shown in Figure 1, this process yielded 200 um-deep TSVs with a diameter of 50 um and sidewall angles ranging from 80° to 90°.

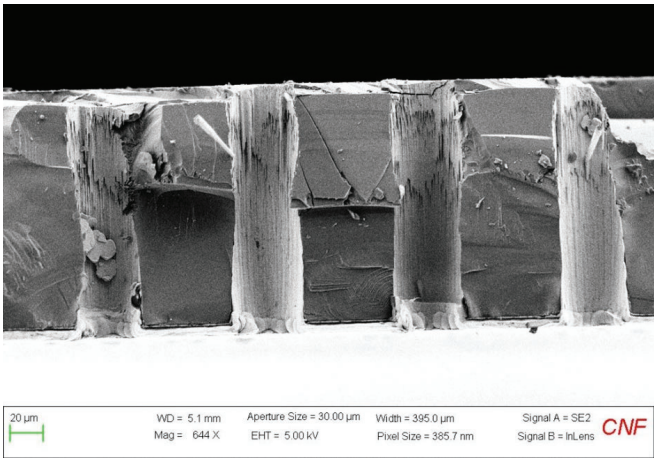

Figure 1: Cross-Sectional SEM Images of TSVs.

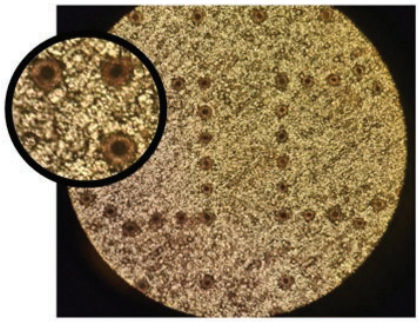

Figure 2: Top-View Optical Image of TSVs After Cu Electroplating.

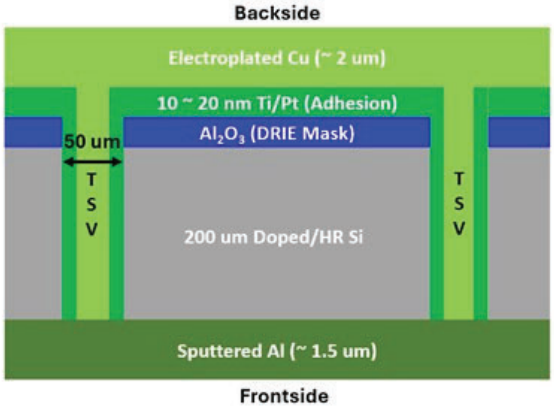

Figure 3: Schematic of Si Interposer Layout.

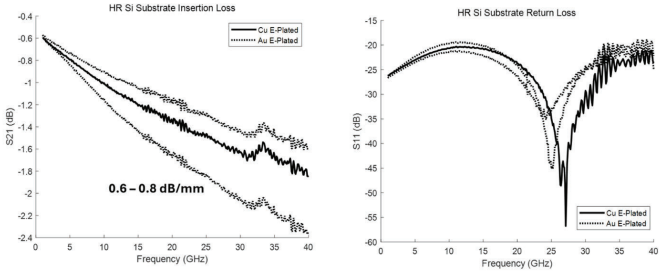

Figure 4: Measured Insertion Loss (S21) and Return Loss (S11) of HR Si Substrate Across 1 – 40 GHz.

After the TSVs were fully etched through, ALD was used to coat the TSV sidewalls with a Pt seed layer. Cu was then electroplated to fill the TSVs, initiating from the Pt seed layer, as illustrated in Figure 2.

Once the backside processing was completed, the front side was patterned with SIW and GCPW lines. A titanium/aluminum (Ti/Al) layer was subsequently deposited using AJA sputter deposition. The structural details and final device configurations are shown in Figure 3.

Both HR and doped Si devices were tested at the High Frequency Test Lab (HFTL) where TSV series resistance and GCPW line performance were evaluated. Using the DC probe station, I-V measurements showed that the TSV series resistance was typically below 1 Ω for both HR and doped Si substrates. RF

measurements were then conducted over 1 – 40 GHz range using the small-signal probe station, as shown in Figure 4. For HR Si, insertion loss (S21) values ranged from 0.6 to 0.8 dB/mm, with return loss (S11) exceeding 20 dB. In comparison, doped Si devices exhibited insertion loss of approximately 3.2 dB/mm and return loss greater than 10 dB.

Conclusions and Future Steps:

The fabrication of Si interposers focused on optimizing Bosch DRIE of thinned Si wafers and refining metallization processes to achieve uniform anisotropic etching and consistent metal filling across the wafer. Measurements comparing HR and doped Si substrates revealed that HR Si exhibits insertion loss an order of magnitude lower than that of doped Si, highlighting its potential as a promising substrate material for millimeter-wave applications. Looking ahead, with updated tools and improved techniques for etching and metallization, fully metal-filled TSVs are expected to achieve insertion losses below 0.5 dB/mm at frequencies up to 220 GHz, utilizing the 220 GHz single-sweep probe station at HFTL.

References:

[1] M. J. Asadi, L. Li, K. Nomoto, Y. Tang, W. Zhao, P. Fay, D. Jena, H. G. Xing, and J. C. M. Hwang, "SiC Substrate Integrated Waveguides for High-Power Monolithic Integrated Circuits Above 110 GHz," 2021 IEEE MTT-S Int. Microw. Symp. (IMS), Atlanta, GA, USA, 2021, pp. 669-672.

[2] D. Malta, E. Vick, S. Goodwin, C. Gregory, M. Lueck, A. Huffman, and D. Temple, "Fabrication of TSV-based silicon interposers," 2010 IEEE International 3D Systems Integration Conference (3DIC), Munich, Germany, 2010, pp. 1–6.

[3] M. Leskela and M. Ritala, Thin Solid Films 409, 138 (2002).

[4] F. Laermer et al., IEEE Microelectromech. Syst. 211 (1999).

Optimizing Silicon Chip Thickness and Pixel Activation Threshold in Scanning Transmission Electron Microscope Detectors

CNF Summer Student: Himani Anilkumar Mishra
Student Affiliation: School of Applied and Engineering Physics, Cornell University

Summer Program(s): 2025 Cornell NanoScale Facility Research Experience for Undergraduates (CNF REU) Program, SUPREME REU

Principal Investigator(s): David A. Muller, School of Applied and Engineering Physics, Cornell University

Mentor(s): Steven E. Zeltmann, Platform for the Accelerated Realization, Analysis, and Discovery of Interface Materials (PARADIM), Cornell University

Primary Source(s) of Research Funding: National Science Foundation under Grant No. NNCI-2025233, SUPREME

Contact: ham74@cornell.edu, steven.zeltmann@cornell.edu, david.a.muller@cornell.edu

Summer Program Website(s): https://cnf.cornell.edu/education/reu

Research Group Website: https://muller.research.engineering.cornell.edu/

Abstract:

Electron ptychography is a scanning transmission electron microscopy (STEM) technique used to achieve high-quality three-dimensional characterization of rapidly shrinking semiconductor devices[1]. We aim to design dose-efficient STEM detectors that use the maximal amount of generated signal. In STEM, a focused beam of electrons are either transmitted and/or scattered by our material of interest. The transmitted electrons then encounter a pixel array detector that is composed of a sensor layer, which is bump-bonded to an ASIC[2,3]. The silicon sensor layer is divided into pixels that record the amount of energy deposited by the electrons. Each pixel has a threshold of activation. If an electron deposits energy greater than the threshold, the pixel is activated. The problem lies in when the electron lands on the intersection of pixels. If the threshold is low, all pixels are triggered, leading to overcounting, but if the threshold is high, no pixels are triggered, leading to undercounting. Therefore, we must find the optimal pixel activation threshold value. We also test different thicknesses for the sensor layer to avoid the problem of oversaturation. We use a Monte Carlo simulation to track the trajectories and energies deposited by an incident beam of electrons in the sensor layer. From this, we analyze energy distributions and calculate the modulation transfer function (MTF) and detective quantum efficiency (DQE)[4,6] to evaluate the performance of different thickness levels and pixel activation thresholds. Careful thresholding in conjunction with thickness optimization will enable dose-efficient STEM for the high-quality characterization of next-generation semiconductors.

Summary of Research:

The pixel array detector is a type of electron microscope detector that offers high-speed data collection due to its parallel pixel readout and sensitivity to signal changes. It is composed of two layers: a sensor layer and CMOS Integrated Chip. The sensor layer is sectioned into square pixels. This layer is then bump-bonded to the IC. When the energy deposited in a given pixel by an electron is greater than the pixel activation threshold value, the pixel is activated. The problem lies in when an electron lands on the intersection of pixels. A low pixel activation threshold will lead to the electron depositing enough energy in all the pixels and activating all of them, resulting in overcounting. A high threshold will lead to the electron not depositing enough energy in any of the pixels and activating none of them, resulting in undercounting.

To study the relationships between sensor layer thickness and pixel activation threshold on the modulation transfer function (MTF) and detective quantum efficiency (DQE) of our system, we modeled the spread of electrons using a Monte Carlo simulation in a 500-micron deep silicon layer. We set varying initial beam voltages, from 60keV to 300keV. We created lateral and depth energy spread distributions, tracking electron energy at each location.

Summing over the Y and Z direction (Z direction is the beam direction, X-Y is the lateral plane) of the silicon, we created a line spread function, plotting the energy as a function of X position. Taking the Fourier transform of the LSF produces the MTF3. Then, we analyze the relationship between different silicon thickness and activation thresholds, performing the simulation for different pairs and plotting the MTF at Nyquist frequency (contrast for the smallest features) and DQE at 0 frequency (noise for the largest features).

We are also interested in studying the behavior of the Timepix4, a thinner detector, with a 300μm-deep Si layer. Using this depth and a 150 keV threshold, we analyze the relationship between beam radius and pixel size. We choose this threshold because it produces a good MTF. A 150 keV threshold corresponds to around 72.7% of the total energy deposition. This energy is contained in a radius of around 244μm, or 4.5 pixels. We map counts for each triggered pixel.

The origin receives the most energy, resulting in the greatest counts. Fewer pixels are triggered near the edge. At a low threshold, a higher ratio of beam radius to pixel width is favored and at high threshold, a lower

ratio of beam radius to pixel width is favored. I also create a pixel activation map for a 300-micron-deep silicon layer (depth of the Timepix4 sensor layer)5, and 150keV threshold and look at the relationship between the initial beam spread and the pixel width.

Conclusions and Future Steps:

Higher initial beam voltages have LSF's with broad tails, as the electrons spread further, both laterally and in depth. Smaller initial beam voltages have sharper LSF's, as the electrons don't have as much lateral or depth spread. Lower beam energies are closer to the ideal MTF because they trigger fewer pixels, producing greater contrast. Lower sensor layer thickness and higher threshold (up to an optimal point) favor higher MTF for the same reason.

Lower thicknesses obtain a better MTF for low thickness, because the electrons' spread is limited, resulting in a smaller radius of energy deposition. Each electron activates only a few pixels, resulting in better contrast. The optimal threshold for a good MTF appears to be around 125 keV for 100, 200, 400 and 500-µm depth, after which point the MTF decreases for higher thresholds. 300-um depth seems to have the optimal MTF around 150keV. Thus, there is an optimal point for the threshold, around 100-150keV, for most thicknesses between 100 to 500 µm.

Meanwhile, DQE is favored by higher sensor layer thickness, because a greater depth allows us to capture the entire spread of the electron, resulting in greater signal acquisition. A higher DQE is also favored by a lower pixel activation threshold because it allows each electron to consistently activate many pixels, producing less noise. At a low threshold, a higher ratio of beam radius to pixel width is favored and at high threshold, a lower ratio of beam radius to pixel width is favored. Thus, MTF and DQE are favored by opposite trends in thickness and threshold. It is important to assess these metrics for each distinct detector design to find the optimal conditions for both metrics. In the future, we will perform the Monte Carlo simulation with more electrons (at least 100,000) for a more detailed understanding of the relationship between thickness and threshold.

We may also consider how detectors with fewer pixels can attain maximal signal capture, as MTF and DQE may be easier to optimize for fewer pixels. Additionally, we can quantify the maximal usable imaging speed (MUIS), in addition to MTF and DQE, to assess different detector designs.

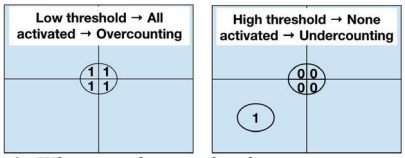

Figure 1: When an electron lands on intersection of pixels, there may be overcounting if the pixel activation threshold is too low and undercounting if the threshold is too high.

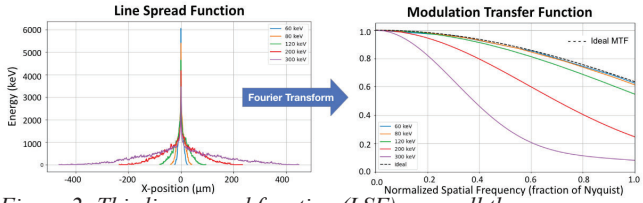

Figure 2: This line spread function (LSF) sums all the energy deposited from 1000 electrons in the Y and Z directions and plots the energy distribution as a function of X position. The Fourier transform of the LSF is the MTF.

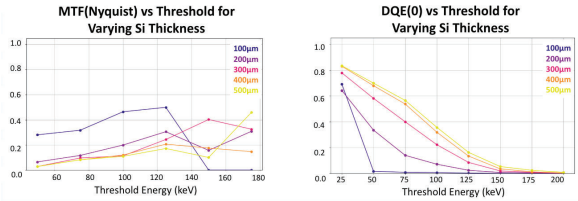

Figure 3: MTF at Nyquist frequency and DQE at zero frequency for varying silicon thicknesses and pixel activation thresholds.

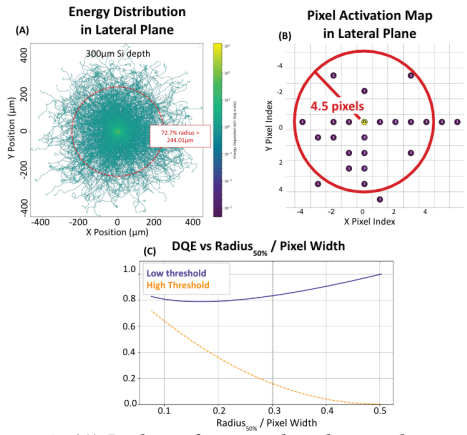

Figure 4: (A) Radius of energy distribution that corresponds to a 150keV threshold. (B) Pixel activation map for 300-µm thick silicon layer. (C) Relationship between ratio of radius where 50% of energy is distributed to pixel width and DQE.

Acknowledgements:

Thank you to my mentor, Steven E. Zeltmann, and Principal Investigator, Professor David Muller for their support and guidance on this project. Thank you to the NSF/SRC SUPREME REU Program and the Cornell Nanoscale Facility (NNCI-2025233) for funding and supporting this project.

References:

[1] S. Karapetyan, S. Zeltmann, T.-K. Chen, V. D. H. Hou, and D. A. Muller, Visualizing Defects and Amorphous Materials in 3D with Mixed-State Multislice Electron Ptychography, Microscopy and Microanalysis 30, (2024).

[2] H. T. Philipp et al., Very-High Dynamic Range, 10,000 Frames/ Second Pixel Array Detector for Electron Microscopy, Microsc Microanal 28, 425 (2022).

[3] M. W. Tate et al., High Dynamic Range Pixel Array Detector for Scanning Transmission Electron Microscopy, Microsc Microanal 22, 237 (2016).

[4] G. McMullan, S. Chen, R. Henderson, and A. R. Faruqi, Detective quantum efficiency of electron area detectors in electron microscopy, Ultramicroscopy 109, 1126 (2009).

[5] N. Dimova et al., Measurement of the Resolution of the Timepix4 Detector for 100 keV and 200 keV Electrons for Transmission Electron Microscopy, Nuclear Instruments and Methods in Physics Research Section A: Accelerators, Spectrometers, Detectors and Associated Equipment 1075, 170335 (2025).

[6] A. Gnanasambandam and S. H. Chan, Exposure-Referred Signal-to-Noise Ratio for Digital Image Sensors, arXiv:2112.05817.

Initiated CVD (iCVD) Polymerization in Liquid Crystal to Synthesize Polymer Particles

CNF Summer Student: Eva Reed
Student Affiliation: Chemical Engineering, Princeton University

Summer Program(s): 2025 Cornell NanoScale Facility Research Experience for Undergraduates (CNF REU) Program, SUPREME REU

Principal Investigator(s): Nicholas Abbott, Rong Yang

Mentor(s): Shiqi Li

Primary Source(s) of Research Funding: Future Manufacturing award to Cornell Chemical Engineering, FMRG: Cyber: Scalable Precision Manufacturing of Programmable Polymer Nanoparticles Using Low-temperature Initiated Chemical Vapor Deposition Guided by Artificial Intelligence, funded by the National Science Foundation under award CMMI-2229092

Contact: ryang@cornell.edu, nla34@cornell.edu, er564@cornell.edu, sl2869@cornell.edu

Summer Program Website(s): https://cnf.cornell.edu/education/reu

Research Group Website: https://theyanglab.com/

Primary CNF Tools Used: Leica 300 CPD, Zeiss Supra SEM

Abstract:

Synthesis schemes targeting specific nanoscale polymer architectures have the potential to advance the efficacy of polymer materials for applications in biomaterials and beyond as tunable material solutions [1]. In our current work, we expand previous investigations of the synthesis pathway of divinylbenzene (DVB) via initiated chemical vapor deposition (iCVD) templated in nematic liquid crystals to begin to explore polymerization with alternative monomers and process conditions. Understanding the effect of tuning the precursor concentrations and substrate properties on the resultant polymer architectures will empower future efforts to produce shape-controlled polymer particles within this synthesis pathway.

Summary of the Research:

Many existing methods to control polymer microparticle architectures involve physical manipulations, which are difficult to scale [1]. Initiated chemical vapor deposition (iCVD) within a liquid crystal (LC) template provides a pathway to construct polymer nanoscale and micro-particles with specific architectures achievable based on the reaction conditions [2]. In iCVD, the polymer precursors–the monomer and initiator–are delivered continuously in vapor phase into a chamber alongside an inert carrier gas. A superheated filament radicalizes the initiator to allow the polymerization reaction to proceed. As the monomer and initiator molecules adsorb onto the substrate, free-radical polymerization occurs. iCVD eliminates the need for solvent-mediated reactions, which can result in impure polymer products, impacting the functionality and applicability of functionalized polymeric materials [3].

The innovation that inspired this project is the use of a liquid crystal (E7, a commodity liquid crystal containing a eutectic mixture of cyanobiphenyls and terphenyls) as a templating material rather than an isotropic (disordered) liquid. Liquid crystals are a phase of matter in between liquid and crystalline solids that acquire exciting and useful properties from heightened orientational and positional ordering of their constituent molecular subunits [5]. Researchers have taken advantage of the molecular level organization in these materials in iCVD systems to guide the polymerization process and control the particles' final conformation [2]. The identity of the substrate on which the film is prepared controls the properties and orientation of the mesogens within the LC thin-film. At the LC-air interface E7 adopts a perpendicular anchoring scheme while at the interface with untreated glass the mesogens will be anchored planarly in multi-domains. Chemical treatments octadecyltrichlorosilane (OTS) and Dimethyloctadecyl(3-(trimethoxysilyl) propyl)ammonium chloride (DMOAP) result in planar anchoring at the LC-substrate surface as well as inducing a single homeotropic domain across the LC film [1]. Representative illustrations of the different anchoring conditions are included in Figure 1. These treatment schemes offer the researcher an additional layer of control to the polymer template during the reaction. In addition to comparing polymer products on substrates with homolayers of OTS, and DMOAP treatments, gradient substrates prepared by the Genzer group at NC State–gradients of OTS to glass, DMOAP to glass,

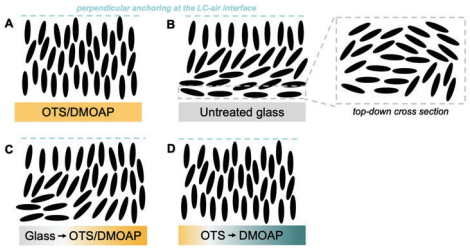

Figure 1: Illustration of anchoring effects on E7 for different substrate types.

and OTS to DMOAP counter gradients–were reacted to provide a comparison of both anchoring condition and the impact of anchoring strength and surface energy [5].

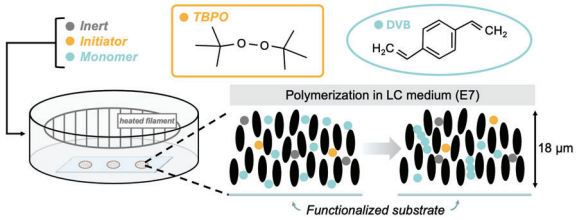

Figure 2: Schematic of in-lab set up for iCVD. Adapted from [1]: Jain, A. Science Advances 2024, 10 (45). https://doiorg/10.1126sciadv.adp5573.

Our experimental system, illustrated in Figure 2, reacts with controlled amounts of vaporized monomer and initiator tert-butyl peroxide (TBPO). The reaction takes place in a TEM grid containing nematic phase liquid crystal films (E7, TNI=60-63°C) mounted on a range of untreated and treated substrates. The chamber pressure is regulated to 150 mTorr and the sample stage is maintained at 20 °C. The reaction process is monitored in situ by a long focal length set up of a Keyence VHX 970F microscope and after reaction progress has been halted by SEM, confocal imaging, and microscopy on an Olympus BX41 microscope equipped with 4× and 20× objectives. Reactions were carried out at both high initiator to monomer ratios (~0.7 Monomer/Initiator) and low ratios (~0.15) at times ranging from 75 to 140 minutes. Critical point drying was employed to remove liquid crystal films while preserving the particles formed for imaging by SEM [1].

Conclusion and Future Steps:

Optical micrographs of films prepared on glass and homolayers of OTS and DMOAP showed that arrays of polymer nanospheres formed with greater regularity and covered a higher percentage of the available film area on DMOAP and glass than the OTS substrate (Figure 3). Analysis of particle sizes showed little significant variation in particle diameter between homolayer substrates: an observation confirmed with SEM imaging of representative polymer particles and particle clusters (Figure 4). Reactions performed on gradient films mirror this trend, with the sections of the film treated with DMOAP displaying a greater proportion of particle arrays than OTS. Analysis of reactions on the OTS to DMOAP gradient film further confirmed this trend, indicating that the anchoring orientation did not impact the formation of particle arrays. An implication of this finding is that the polymerization process occurs in the bulk LC or at the LC-air interface rather than on the LC-substrate interface. This hypothesis was supported by confocal microscopy which revealed that the nanosphere particles were positioned along a single focal plane within the LC bulk.

Determining the location of particle formation during the initiation and growth processes deepens knowledge of the dynamics of the polymerization reaction and,

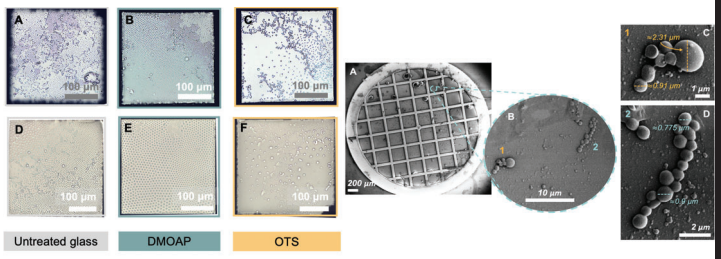

Figure 3 (Left) : White balanced optical micrographs showing the polymer products formed from high initiator to monomer ratio conditions (17.1 mTorr P(TBPO)/25.1 mTorr P(DVB)) (A-C) and low initiator to monomer ratio conditions (10.6 mTorr P(TBPO)/69 mTorr P(DVB)) (D-F). The DMOAP treated films (B,E) create more regular particle arrays than the untreated glass films (A,D) or the OTS treated films (C,F).
Figure 4 (Right): SEM images showing polymer nanoparticles. Low magnification (A) and high magnification are shown (B) alongside measurements of the range of particle diameters are also displayed (C, D).

in turn, will offer researchers greater insight into controlling the polymer architectures formed within the LC films. Future work will bring in more advanced imaging and characterization techniques, including AFM and advanced confocal microscopy, to detail this polymerization process and allow our understanding to empower iCVD studies of other monomer systems.

Acknowledgements:

This work was performed in part at the Cornell NanoScale Facility, a member of the National Nanotechnology Coordinated Infrastructure (NNCI), which is supported by the National Science Foundation (Grant NNCI-2025233). This work is further funded by a Future Manufacturing award to Cornell Chemical Engineering, FMRG: Cyber: Scalable Precision Manufacturing of Programmable Polymer Nanoparticles Using Low-temperature Initiated Chemical Vapor Deposition Guided by Artificial Intelligence, funded by the National Science Foundation under award CMMI-2229092 and finally the NIH S10RR025502 grant to the BRC for the Zeiss LSM 710 confocal microscope.

References:

[1] Jain, A et al., Single-step synthesis of shaped polymeric particles using initiated chemical vapor deposition in liquid crystals. Sci. Adv. 2024 10, eadp5573. DOI:10.1126/sciadv.adp5573..

[2] Cheng, Z.; Lee, H.; Kim, T.; et al. Templated Nanofiber Synthesis via Chemical Vapor Polymerization into Liquid Crystalline Films. Science 2018, 360 (6391), 804–808. https://doi.org/10.1126/science.aar8449

[3] Bradley, L. C.; Gupta, M. Microstructured Films Formed on Liquid Substrates via Initiated Chemical Vapor Deposition of Cross-Linked Polymers. Langmuir 2015, 31 (29), 7999–8005. https://doi.org/10.1021/acs.langmuir.5b01663.

[4] De Luna, M. S.; Torres, C. A.; Chen, H.; et al. Interactions between Polymers and Liquids during Initiated Chemical Vapor Deposition onto Liquid Substrates. Mol. Syst. Des. Eng. 2020, 5 (1), 15–21. https://doi.org/10.1039/c9me00087a.

[5] Clare, B. H.; Efimenko, K.; Fischer, D. A.; Genzer, J.; Abbott, N. L. Orientations of Liquid Crystals in Contact with Surfaces That Present Continuous Gradients of Chemical Functionality. Chem. Mater. 2006, 18 (9), 2357–2363. https://doi.org/10.1021/cm052537n.

Alpha-Tantalum Thin Film Deposition on Pure Silicon Wafers with the Angstrom-Q

CNF Summer Student: Porter Rowbotham
Student Affiliation: Mechanical Engineering, Rochester Institute of Technology

Summer Program(s): Summer 2025 CNF NORDTECH Intern
Mentor(s): Aaron Windsor - Thin Film Process Engineer, CNF
Primary Source(s) of Research Funding: NORDTECH
Contact: pjr4887@rit.edu
Research Group Website: https://www.nordtechub.org
Primary CNF Tool Used: Angstrom-Q, Filmetrics R50, Zeiss Ultra SEM

Abstract:

Material choice in superconducting quantum circuits can greatly impact device coherence and losses. Recently, Tantalum thin films have shown great potential for transmon qubit fabrication, boasting high resonating times and high quality[1]. Tantalum's α crystal phase is especially important as it boasts a superconducting critical temperature of 4.2°K. Recent studies have shown that using a heated substrate can enable α-Tantalum thin film deposition [2,3,4]. The Cornell Nanoscale Facility recently introduced a new quantum-oriented electron beam evaporation tool witwh the capabilities to deposit these films, the Angstrom-Q. The project for this summer is to find the transition temperature where α-Tantalum can be deposited.

Summary of Research:

All samples for this project are deposited on 100mm undoped silicon wafers. All Tantalum depositions are completed at 1Å/s to a final thickness of 500Å.

Deposition Temperatures:

The temperature at which deposition takes place across different tools for α-Tantalum deposition can vary greatly based on the temperature measurement or deposition method. Sputtering an α-tantalum film may require a higher heat than evaporation as evaporation's particles carry heat onto the surface of the substrate. With studies showing α-Tantalum growth at 350°C [2], 400-500°C[3], and 600-650°C[4]. With this data, we chose to do a baseline run at room temperature, and then start at 350°C, moving at 50°C increments until the transition temperature is found, then move to 10°C increments.

Wafer cleaning:

One of the most important steps in creating a high quality α-Ta film is the cleaning. The wafers are RCA cleaned at the CNF MOS tanks, followed by a 60s bath in 20:1 HF to remove any surface oxides. This process remained until a water-streaked, highly non-uniform film began to appear at deposition temperatures above 425°C. We suspected that the HF bath in the MOS bath may be contaminated, or that the wafer was being oxidized by spending too long being rinsed in DI water. To correct this, we switched to removing the surface oxides by using 10:1 HF for 60s and 30s dip in DI water by hand. Additionally, it was found that the samples should spend less than one hour between the finish of the MOS clean and being processed.

Heated Deposition:

Once the wafer is fully cleaned and has its surface oxides stripped, it is placed in the Angstrom-Q load lock and put under vacuum. This is done in less than ten minutes to avoid the re-growth of surface oxides. Once in the machine, the wafer is heated to the desired deposition temperature, and then held at that temperature for 60 minutes to ensure even heating across the substrate. The wafer and carrier are allowed to cool and removed once reaching a temperature lower than 100°C.

Resistivity:

One convenient method to determine the crystallinity of a tantalum film is the film's resistivity. The room temperature resistivity of β-Ta is 150-200μΩ-cm and the resistivity of α-Ta is 15-20μΩ-cm [3]. We used the Filmetrics R50 four point probe to measure the sheet resistance of the film, then multiplied the sheet resistance by the thickness of the film to find the resistivity of the samples (Figure 1).

X-Ray Diffraction:

X-Ray Diffraction (XRD) scans were completed on all of the samples using the Rigaku SmartLab X-ray Diffractometer at the Cornell Center for Materials Research by Lingda Kong. Matching known scan peaks to our experimental runs shows what crystalline phase the sample is (Figure 2).

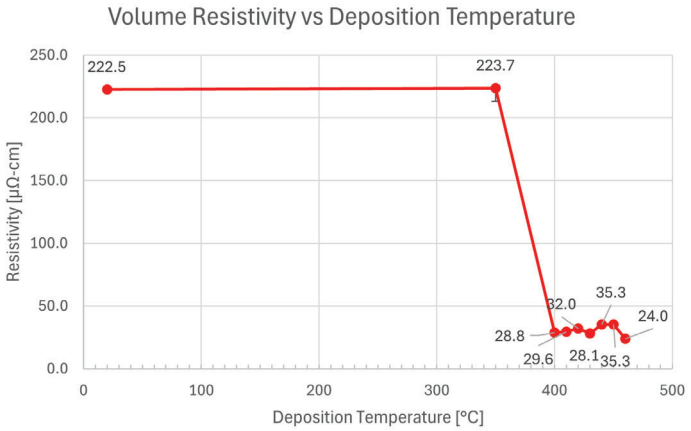

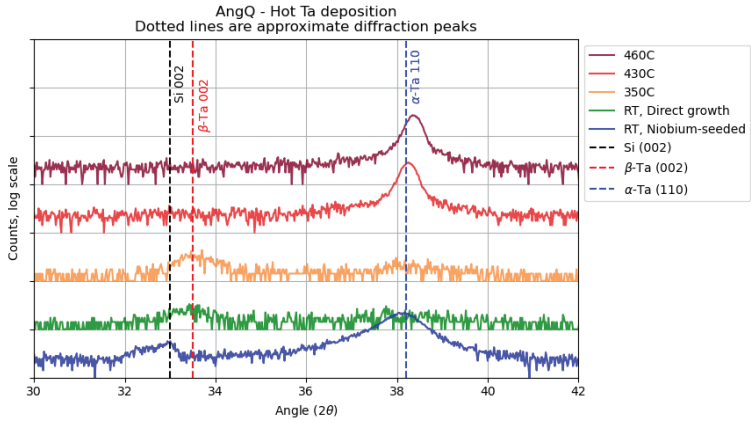

Figure 1 (Left): Volume Resistivity of Samples vs. their Deposition Temperature. Figure 2 (Right): X-Ray Diffraction Scans of Several Samples

Seed Layers:

A popular method for growing an α-Tantalum film is to use a thin layer of another material to avoid Tantalum-Silicon interactions and promote the correct crystalline phase. We did one Niobium seeded Tantalum deposition with 5Å of Niobium and 50Å of Tantalum, both deposited at 1Å/s at room temperature. The niobium seed layer sample had a RT resistivity of 60.8μΩ-cm. XRD scanning showed a peak around the α-Tantalum region without a peak in the α-Tantalum range (Figure 2).

Conclusions and Future Steps:

With this data, we can conclude that mostly pure α-Tantalum depositions on pristine silicon wafers at temperatures above 400°C, and that the transition temperature may lay in the 350-450°C range. Niobium seeded tantalum deposition shows α-Tantalum results at room temperature. Further depositions could be used to find the exact temperature range to form pure α-Tantalum. Additionally, films should be investigated to see if Tantalum Silicides (TaSi2) are being formed. Once completed, quantum computing components could be fabricated.

Acknowledgements:

Special thanks to NORDTECH and the Cornell Nanoscale Facility for funding and hosting this internship. Thanks to my CNF staff mentor Aaron Windsor, and CNF staff Shilling Du for their help and guidance. Thanks to Fatemi Lab, and its members Lingda Kong and Tathagata Banerjee for all of their helpful insights and guidance.

References:

[1] A.P.M. Place, L.V.H. Rodgers, P. Mundada et al. "New material platform for superconducting transmon qubits with coherence times exceeding 0.3 milliseconds," Nat Commun 12(1), (2021).https://doi.org/10.1038/s41467-021-22030-5

[2] G. Marcaud, D. Perello, C. Chen, et al. "Low-Loss Superconducting Resonators Fabricated from Tantalum Films Grown at Room Temperature," (2025). https://doi.org/10.48550/arXiv.2501.09885

[3] D.P. Lozano, M. Mongillo, X. Piao, et al. "Low-loss α-tantalum coplanar waveguide resonators on silicon wafers: fabrication, characterization and surface modification," Mater. Quantum. Technol. 4(2), 025801 (2024).https://doi.org/10.1088/2633-4356/ad4b8c

[4] 1 M.P. Bland, F. Bahrami, J.G.C. Martinez, et al. "2D transmons with lifetimes and coherence times exceeding 1 millisecond," (2025).

Structure and Dynamics of the Compression Induced Polycrystalline-Glass Transition

CNF Summer Student: Sylvie Shaya
Student Affiliation: Wellesley College Department of Physics

Summer Program(s): 2025 Cornell NanoScale Facility Research Experience for Undergraduates (CNF REU) Program, SUPREME REU

Principal Investigator(s): Julia Dshemuchadse, Erin Teich

Mentor(s): Katherine Wang

Primary Source(s) of Research Funding: National Science Foundation award NNCI- 2025233

Contact: jd732@cornell.edu, et106@wellesley.edu, xw682@cornell.edu, ss131@wellesley.edu

Summer Program Website(s): https://cnf.cornell.edu/education/reu

Research Group Website: https://capecrystal.mse.cornell.edu/

Abstract:

When polycrystal grain size is sufficiently reduced, materials undergo a solid-to-glass transition that is distinct from the more commonly studied liquid-to-glass transition and is critical to understanding the behavior of ultrafine-grained polycrystals. These materials hold promise in microelectronics and thermoelectrics, yet their behavior at and beyond the glass transition is not well understood. We simulate a binary system of hard and soft particles under compression to investigate the structure and dynamics of the polycrystalline-to-glass transition. Our results reveal a strong relationship between local structural features and dynamical behavior and indicate that soft particles play an outsized role in the glass transition, as they are associated with areas of strong dynamics and disorder.

Summary of Research:

Background:

Polycrystals are known to exhibit Hall–Petch behavior, which describes how materials strengthen as grain size is reduced. As grain size is further decreased and grain boundary behavior dominates, polycrystals soften and become glassy [1]. Ultrafine-grained polycrystals display properties of interest for materials applications, including high electrical conductivity and reduced thermal conductivity, and understanding the polycrystalline-to-glass transition is critical for further development of these materials [2].

Simulation Methods:

We perform molecular dynamics simulations on a binary system of 6400 hard and 6400 soft discs using the simulation toolkit HOOMD-blue [3]. Particle interactions were defined by Weeks–Chandler–Andersen potentials shifted radially to ensure all particles have the same effective diameter of $d = 1$, with Lorentz–Berthelot mixing rules applied to cross-interactions, described in Fig. 1(b). Particle softness was denied via σ, which varies the shape of the potential well. Hard-particle softness was defined as $\sigma = 0.2$ and held constant for all systems, and soft- particle softness was varied between $\sigma_{soft} = 1$ and 5, as shown in Fig. 1(a).

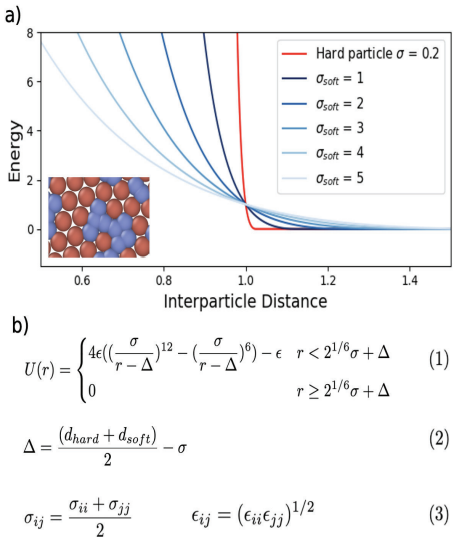

Figure 1: Model setup. (a) Particle interactions via Weeks–Chandler–Andersen potentials for various softnesses σ. (b) Equations describing particle interactions. 1.) Weeks–Chandler–Andersen potentials, shifted radially by a factor Δ, defined in equation 2.). 3.) Lorentz–Berthelot mixing rules.

The system was initialized at low density, then randomized and compressed to a density between $\phi = 0.8$ and $\phi = 1.1$. Following compression, the system was equilibrated to account for artifacts from the compression step, then run for 10^8 molecular dynamics timesteps to collect data. Simulation temperature was fixed at $kT = 0.2$.

Results:

To establish the system's glassiness, we investigate the mean squared displacement (MSD) and the non-Gaussian parameter α(t), an indicator of dynamical heterogeneity. Glassy systems feature a plateau in MSD and a peak in α(t) at intermediate time scales, due to particles being trapped in cages of their neighbors before moving collectively at long time scales [4]. At low σ_{soft}, the system is crystalline and shows neither of

these features. We chose to focus on σsoft = 4, where we observe these behaviors at ϕ-values above 0.9, indicating that the system is glassy.

The compression of the system can be seen in the radial distribution functions (RDFs), where hard–soft and soft–soft RDF peaks are broader and located at smaller distances *r* than hard–hard peaks, seen in Fig. 2(a), as soft particles overlap under compression. There are clear peaks in the RDF at low ϕ, which disappear under compression, as shown in Fig. 2(b), reflecting the existence and subsequent breakdown of long-range order as the system transitions into a glass.

Lattice structure was characterized through the hexatic order parameter ψ_6. Global ψ_6 is maximal (at 1) when the system is crystalline, and decreases at higher ϕ, shown in Fig. 2(c). At high densities, the distribution of soft particle ψ_6 is flatter than that of hard particles, seen in Fig. 2(d), indicating that soft particles tend to be more disordered than hard particles.

To characterize the dynamics of the system, we calculate the Lindemann parameter *L*, a measure of the strength of particle dynamics, and D²min, an indicator of irreversible rearrangements [1, 5]. At low densities, particles with large *L* and D2min exist primarily along grain boundaries. As density increases, high *L* and D²min particles form clusters throughout the system, as seen in Figs. 3(a)-(b). The distribution of soft-particle *L*s and D²min is higher than those of hard particles, seen in Figs. 3(d)-(e), indicating that soft particles display stronger dynamics than hard particles.

To understand the relationship between dynamical parameters and structure, we calculated the covariances of D2min with the number of soft neighbor particles and *L* with ψ_6, shown in Fig. 4(a)-(b). For $\sigma_{soft} = 4$, there is a peak at $\phi = 0.9$ for both covariances. The peak of the covariance of *L* and ψ^6 has been shown to correlate to the polycrystalline-to-glass transition [1]. We observe a peak in the same location in the covariance of D²min and number of soft neighbors, in Fig. 4(b), demonstrating a clear relationship between structure and dynamics at the glass transition.

As σ_{soft} increases, the peak of the covariance, and in turn the glass transition, shifts lower in density, seen in Fig 4(b). The global average ψ_6 shifts similarly, as seen in Fig. 2(c), as the breakdown in structure associated with the glass transition shifts.

Conclusion and Future Steps:

Under compression, binary systems of hard and soft particles display interesting behavior as they undergo a polycrystalline-to-glass transition. There is a strong relationship between the structure and dynamics of the system, seen in the covariances of dynamical and structural properties. Soft- particle softness impacts the location of the glass transition in density space, and soft particles appear to play an outsized role in this transition, as they tend to have stronger dynamics and disorder than hard particles.

Future steps include improved characterization of the relationship between structure and dynamics through statistical analysis, and descriptions of the collective motion of particles. Qualitative observation of the system indicates the existence of string- and loop-like cooperative motion, which in future work could be related to the structure of the system.

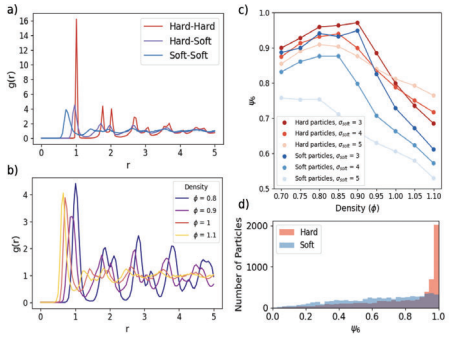

Figure 2: Structural parameters. (a) Type-wise RDFs for the 100th frame of simulations with $\sigma_{soft} = 4$ and $\phi = 1$. (b) Soft–soft RDFs for $\sigma_{soft} = 4$ over various ϕ values. (c) Global average ψ_6 for hard and soft particles. (d) Distributions of ψ6 by particle type at the 100th frame of simulations with σsoft = 4 and $\phi = 1$.

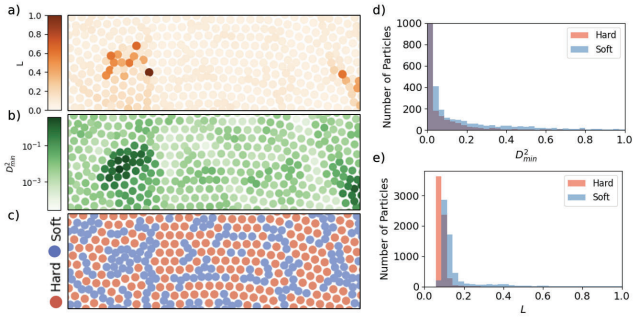

Figure 3: Dynamical characterizations, calculated over the first 100 frames of simulations with $\sigma_{soft} = 4$ and $\phi = 1$. (a) Heatmap of L. (b) Heatmap of D^2_{min} with a logarithmic colormap. (c) Particle identities at the 100th frame of simulation. (d) Histogram of L by particle type. (e) Histogram of D^2_{min} by particle type.

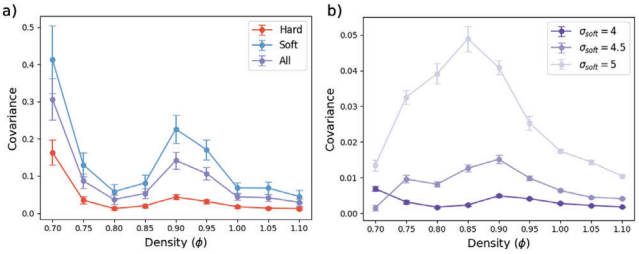

Figure 4: Covariances of dynamics and structure. (a) Typewise covariances of D^2_{min} and number of soft particle neighbors for $\sigma_{soft} = 4$. (b) All particle covariances of disorder, defined as $1-\psi_6$, and L over various σsoft values.

References:

[1] Zhang, H. & Han, Y. Physical Review X 8, 041023 (2018).

[2] Lu, L. et al. Science 304, 422–426 (2004).

[3] Anderson, J.A. et al. Computational Materials Science 173, 109363 (2020).

[4] Teich, E.G. et al. Nature Communications 10, 64 (2019).

[5] Falk, M.L. & Langer, J.S. Physical Review E 57, 7192 (1998).

Computer Vision Applied to Polymer Particles in Liquid Crystal (LC) to Enable On-the-Fly Characterization of their Morphology and Size Distribution, Among Other Properties

CNF Summer Student: William Sober
Student Affiliation: Physics, Amherst College

Summer Program(s): 2025 Cornell NanoScale Facility Research Experience for Undergraduates (CNF REU) Program, SUPREME REU

Principal Investigator(s): Nicholas Abbott, Fengqi You

Mentor(s): Soumyamouli Pal

Primary Source(s) of Research Funding: National Science Foundation award NNCI- 2025233, Center for Energy Efficient Magnonics (DE-AC02- 76SF00515), Department of Energy Office of Science, Basic Energy Sciences (DE-SC0019997)

Contact: nla34@cornell.edu, fengqi.you@cornell.edu, willsober@gmail.com

Summer Program Website(s): https://cnf.cornell.edu/education/reu

Abstract:

Monitoring polymerization reactions in-situ provides many advantages like real-time feedback for tuning conditions and viewing undisturbed growth. However, image quality can be reduced due to difficulties in viewing the reaction such as vibrations and long working distances with a microscope. This project explores approaches to enhance lower quality in-situ microscope images of polymers in liquid crystal from an initiated chemical vapor deposition (iCVD) reactor by using an enhanced super resolution generative adversarial network (ESRGAN). To train ESRGAN, polymer test systems were set up in an iCVD reactor, and low-quality in-situ images of the polymers were taken along with corresponding high-quality ex-situ images. We cropped matching single-cluster images and applied different pre-processing techniques while varying hyperparameters such as learning rate and weight decay. The accuracy of these methods was evaluated with the Structural Similarity Index Measure (SSIM) and visually compared to the reference high-quality images. We found that overall, ESRGAN has strong potential for polymer image enhancement, and changeable hyperparameters gives it versatility for different images. However, further model optimization is needed before it is adapted for real polymerization images. The adaptability of ESRGAN makes this approach applicable for more varied use like new types of polymers or different microscope setups.

Summary of Research:

Initiated chemical vapor deposition (iCVD) in liquid crystal (LC) has the capability to produce tunable polymer growths like nanospheres with potential for use in drug delivery or separations for chromatography1. In-situ monitoring of the reaction is possible through a window with a long-distance focal length lens Keyence VHX 970F microscope. However, issues with vibrations and external noise are compounded by the viewing distance, so the images from the microscope are blurry and low-quality. The samples can be high-quality ex-situ imaged by an Olympus BX41 microscope although this requires stopping the reaction to remove samples, which can also disturb polymers.

With the assistance of a machine learning-based approach, we can enhance the in-situ images to more closely match the quality of the high-quality ex-situ images. Previous preliminary research has found that the enhanced super-resolution generative adversarial networks (ESRGAN) model outperforms other models for this purpose.

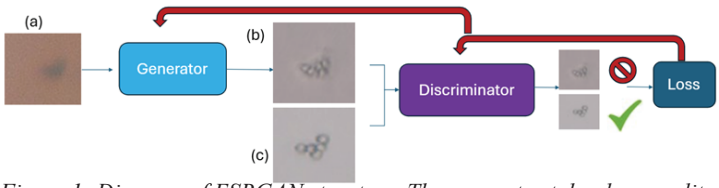

Figure 1: Diagram of ESRGAN structure. The generator takes low-quality images (a) and enhances them (b). The discriminator detects real (c) from fake images and then model updates from loss functions.

ESRGAN has two key components: the generator and the discriminator (Figure 1). For training, the generator takes a low-quality image and tries to enhance it to look like a high-quality image. The discriminator is then given that enhanced image along with the actual high-quality image and tries to determine which is the real one. Then the model calculates loss functions for how poorly the generator and discriminator performed so that the generator and discriminator can improve their weights. This process is iterative, with the generator and discriminator improving each other thousands of steps. In

addition to the images used for training, many are set aside solely for testing the performance of the model to limit overfitting.

We tried multiple configurations of ESRGAN by varying hyperparameters, which are parameters in ESRGAN that can be adjusted to change how the model learns. We mainly looked at learning rate (.0001-.001), weight decay (0 or .0001), and number of epochs(10-300).

A test system was created using commercially available 5µ polystyrene spheres dispersed in the liquid crystal, allowing for fixed particle sizes and faster data collection compared to growing polymers.

Training the model with images of the entire LC grid causes complications with identifying the same polymer across low and high-quality images, therefore we used 64x64 pixel cropped patches, 32x32 pixel downscaled cropped patches, and 64x64 images where the contour of the particle was cropped and the background was replaced with white (Figure 2).

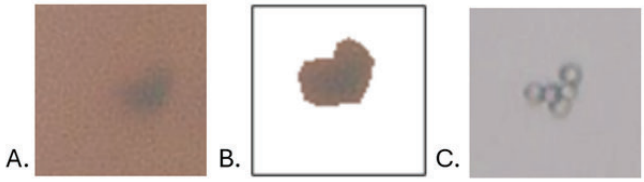

Figure 2: A. Low quality cropped polymer cluster, with B. its contour cropped and C. their high-quality reference. These images were used as three different training inputs for ESRGAN.

Conclusions and Future Steps:

As an exploratory project, a main goal of this project was to explore the feasibility of different approaches. Weight decay stabilized training of the 64x64 images and produced best overall results. Conversely, with 32x32 images, removing weight decay allowed the model to make riskier, but successful, improvements. While contour cropping the particles was not effective, ESRGAN was generally robust against noise. The main limitation was particle size estimation accuracy (Figure 3), likely due to inconsistent scaling during preprocessing. Remaking the dataset may resolve this issue. Overall, these findings establish a strong foundation for adapting ESRGAN for polymerization imaging.

For future development, ESRGAN should be adapted to work on real polymerization images, and polymers of different sizes. Training on lower magnification images would be more effective at capturing more polymers in the frame, fitting six full grids into the frame instead of one. Implementing the model with video capabilities would aid in faster and more convenient analysis during reactions. Applying a different de-noising program to the low and high quality images could also potentially increase the ground truth image quality and accelerate training.

References:

[1] Apoorva Jain et al., Single-step synthesis of shaped polymeric particles using initiated chemical vapor deposition in liquid crystals. Sci. Adv. 10,eadp5573(2024).DOI:10.1126/sciadv.adp5573

Characterization of Silicon Oxide Etching with Low Global Warming Potential Hydroolefin

CNF Summer Student: Elyas Talda
Student Affiliation: Rochester Institute of Technology

Summer Program(s): 2025 Cornell NanoScale Facility Research Experience for Undergraduates (CNF REU) Program
Mentor(s): Jeremy Clark , Cornell NanoScale Science and Technology Facility, Cornell University
Primary Source(s) of Research Funding: National Science Foundation under Grant No. NNCI-2025233,
Contact: clark@cnf.comell.edu, ehtalda@gmail.com
Summer Program Website(s): https://cnf.cornell.edu/education/reu
Primary CNF Tools Used: Gamma Automatic Coat-Develop Tool, ASML PAS 5500/300C DUV Wafer Stepper, P7 Profilometer, Zeiss Ultra SEM, Zeiss Supra SEM, Oxford 82 Etcher, Oxford 100 ICP-RIE Dielectric Etcher, YES EcoClean Asher, and Thermal Oxidation Furnace

Abstract:

The semiconductor industry utilizes hydrofluorocarbons (HFCs) for many different etch processes. HFCs, however, have high global warming potential (GWP). The American Innovation and Manufacturing Act of 2020 enabled the U.S. EPA to scale down the use and production of HFCs. Hydroolefins (HFOs), originally created by the refrigerant industry to reduce reliance on HFCs, show promise as an etch gas in reactively ion etched (RIE) anisotropic etching. This work explores the optimal etch conditions of

HFO-1234ze(E), or $C_3H_2F_4$ on the Oxford PlasmaLab 100 Inductively Coupled Plasma Reactive Ion Etcher. Etch rates remained similar to other oxide etch chemistries, though RIE lag remains a concern, especially with higher concentrations of $C_3H_2F_4$ in the plasma. Deposition and delamination occurred occasionally in the process of characterization, when $C_3H_2F_4$ concentration was too high or the DC voltage bias became too low. $C_3H_2F_4$ holds promise for regular use as a silicon oxide etch gas with more characterization and process research.

Summary of Research:

Silicon oxide is a common etch material in the semiconductor industry and is often etched with hydrotluorocarbons (HFCs) for their versatility and availability1. Though HFCs are not ozone-depleting, they have high global warming potentials (GWP), contributing to global warming in the atmosphere. The AIM Act of 2020 allowed the EPA to begin the scale down in use and production of HFCs, creating a need in the semiconductor industry for new silicon oxide etch gases. HFO-1234ze(E), or $C_3H_2F_4$ has shown potential in silicon etching but it has not been characterized definitively1,[2]. A broad analysis was thus conducted to test the etch rate, selectivity, sidewall angle, and RIElag of various etch recipes of $C_3H_2F_4$. RIElag is the effect of smaller features etching at a slower rate to larger features. It can be reduced by altering the properties of an etch plasma. The Oxford PlasmaLab 100 was used to characterize $C_3H_2F_4$ since, as an ICP etcher, it allowed the individual control of multiple different parameters, controlling the plasma both chemically and physically. Patterned and blank silicon oxide wafers were tested on the Oxford 100 over the course of the experiments.

About 1 micron of silicon oxide grown on Silicon test wafers in a wet oxide furnace. Most wafers were patterned using the Gamma Automatic Coat-Develop Tool, though some wafers were hand-spun, replicating the Gamma processes. BARC was spun on wafers for 30 seconds at 2400 rpm, before a 60-second, 205° bake. Next, UV210-0.6 photoresist was spun at 2900 rpm for 30 seconds, with a 60-second, 135° bake. The wafers were patterned using the ASML PAS 5500/300C DUV Wafer Stepper. Two patterns were used, a standard edge-clear pattern and the ALE Test Mask for RIElag that has trenches of varying width, from 5 micron to 300 nm, with large additional corner features. Finally, the wafers were developed with a 135° bake for 90 seconds, before a 60-second 724MIF develop.

Every patterned wafer had an BARC removal with a I-minute, 45-second ARC etch on the Oxford 82. After, step height of the large corner features was measured with the P7 Profilometer using a shortened version of a pre-existing sequence, testing 10 different comers. Each wafer was etched in the Oxford 100. Prior to each etch, the Oxford 100 was cleaned and seasoned for 2 minutes with either a bare silicon wafer or a blank silicon oxide wafer, to test for deposition. After etching in the Oxford 100, the P7 sequence was run again before the wafer was cleaned with a 5-minute photoresist-strip recipe on the YES EcoClean Asher. A last step height measurement was taken with the P7 sequence. Each relevant wafer's

depth and sidewall angle of the largest and smallest feature was measured using the Zeiss SEM Ultra. Wafers with deposition etches were measured for the height of the deposition. Wafers that delaminated or etched less than 40 nm of silicon oxide were not measured on the SEM.

Table 1: Initial Characterization Etches and Results.

Etch Recipe and Time	Oxide Etch Rate (nm/min)	Selectivity Oxide:Resist	Avg. Sidewall Angle	RIELAG
$C_3H_2F_4$ High He (2 min)	217	6.3	95	0.72
CH_2F_2/High He (116 sec)	156	2.8	98	0.80
CHF_3/O2 Oxide (2 min)	168	1.7	93	0.83
C_4F_6/High He Oxide (2 min)	261	1.4	135	0.98
5 sccm CH_2F_2, 40 sccm C_4F_6, 3 sccm C_4F_8, 20 sccm Ar (2 min)	231	1.9	127	0.98

Table 2: Final Experiment Parameters

Parameter	Min	Max
ICP (W)	1500	2500
RIE (W)	40	80
Pressure mTorr	4	8
Gas Ring	Off	On
$C_3H_2F_4$ (sccm)	10	30
He (sccm)	20	90
Ar (sccm)	0	50

Table 1 (Left): The five etches used and their resulting etch rates.
Table 2 (Right): Final Experiment Parameters.

A round of characterization etches compared the capabilities of the given $C_3H_2F_4$ recipe to that of other common silicon oxide etch recipes. Table 1 shows the five etches used and their resulting etch rate, selectivity, and RIElag. RIElag was calculated by the ratio of the smallest feature's depth to the largest feature's depth; the closer the value to 1, the less lag in etch rate of smaller features. The results confirmed that $C_3H_2F_4$ held potential as a silicon oxide etch gas. It had similar results in etch rate and sidewall angle, which was measured as the inside angle from the etched depth to the sidewall. Selectivity was improved from the other etches, but RIElag was worse. Thus, RIElag was the focused goal of continuing experimentation with additional goals of staying on target with selectivity, etch rates, and sidewall angle.

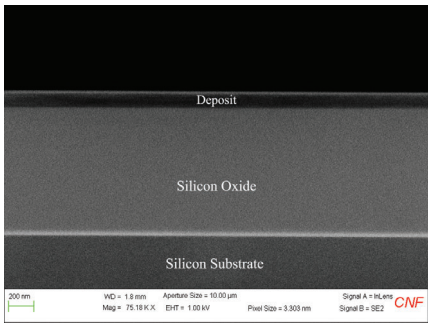

Figure 1: Deposition wafer.

Next, an experiment was designed using the JMP DOE software to find the optimal way to characterize multiple parameters within the etch recipe in a minimum number of wafers. The initial parameters used were the chamber pressure, the RF power, the ICP power, the usage of the gas ring to dispense $C_3H_2F_4$, and the concentration of $C_3H_2F_4$ to Helium. The experiment, however, immediately resulted in much deposition instead of etching. The experiment was ended to allow for more characterization attempts with blank silicon oxide wafers to determine better value ranges for each parameter. Many of these characterization attempts resulted in deposition, with some wafers having nearly 400 nm of C_2F_4 deposited in 2 minutes, and delamination, slowly approaching more appropriate value ranges. A deposition wafer is shown in Figure 1. From this characterization, it was determined that high concentrations of $C_3H_2F_4$ and low DC voltage bias were likely causes of deposition.

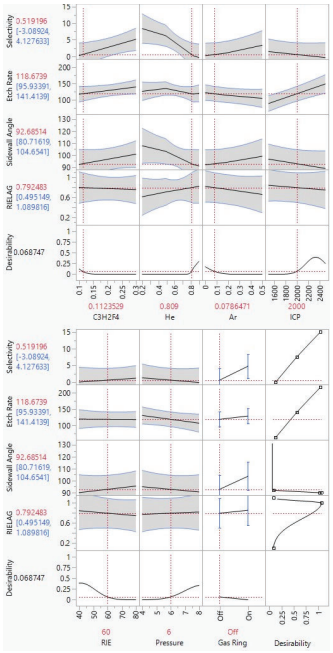

Figure 2: Results from Argon addition.

A secondary experiment design was created with JMP DOE. The modified parameters are shown in Table 2. Argon was added to the process to determine its influence. 20 wafers were run through this experiment. The results were formatted into a fit model and are shown in Figure 2. Etch rates ranged from 10 nm/min to 211 nm/min. Selectivity and sidewall angle remained on target with other silicon oxide etch recipes. RIElag varied with only a few recipes improving from the original's capability. From the results, it is evidenced that lower concentrations of $C_3H_2F_4$ with higher concentrations of Helium result in the best etch rate, RIElag, and sidewall angle. It should also be noted that there is a connection between increased RIE power and decreased RIElag, which would be a site for future research to build on. Though the results of this study were broad, they support further research and characterization on $C_3H_2F_4$ for future use across the semiconductor industry as a low GWP silicon oxide etch gas.

References:

[1] Windsor, Aaron J., Jeremy C. Clark, George McMurdy, Eric A. Joseph, Robert G. Syvret, Ronald J. Olson, and Judy J. Cha. 2025. "Viability ofHFO-1234ze(E) (Trans-1,3,3,3-tetrafluoropropene) as a Low Global Warming Potential Silicon Dioxide Etch Gas." Journal of Vacuum Science & Technology B Nanotechnology and Microelectronics Materials Processing Measurement and Phenomena 43 (2). https://doi.org/10.1116/6.0004194.

[2] H. Omori, A. Kikuchi, A. Yao and I. Mori, "Evaluation of etching property in C3HXF(6-X) plasma," 2016 IEEE 16th International Conference on Nanotechnology (IEEE-NANO), Sendai, Japan, 2016, pp. 127-130, doi: 10.1109/NANO.2016.7751309.

AJA Sputter 1 & 2 Materials Characterization

CNF Summer Student: Irwin Wang
Student Affiliation: Department of Engineering, Cornell University

Summer Program(s): 2025 Cornell NanoScale Facility Research Experience for Undergraduates (CNF REU) Program
Mentor(s): Tom Pennell, Cornell NanoScale Science and Technology Facility, Cornell University
Primary Source(s) of Research Funding: National Science Foundation under Grant No. NNCI-2025233,
Contact: iw87@cornell.edu, tjp83@cornell.edu

Abstract:

The application of sputtering for thin-film deposition has been a staple technique for decades, and its importance is growing with the expansion of nanotechnology. As new materials are developed to address unique challenges, their characterization within sputtering tools becomes increasingly essential. This study investigates the effects of various sputtering conditions on key film properties. The primary objective was to understand the relationship between sputtering parameters and both film Deposition Rate and Film Stress, while also measuring secondary characteristics such as Sheet Resistance and Index of Refraction. Depositions were performed using AJA 1 and AJA 2 Sputtering machines. The primary variable was chamber pressure, tested at three levels: 3 mTorr, 7 mTorr, and 20 mTorr. Deposition times were controlled to achieve a target film thickness between 100-300 nm for all samples. For a range of previously uncharacterized materials (Zr, Nb, Ru, Si3O4, Hf, NiO), trends for deposition rate and film stress were consistent with existing data. Specifically, increased chamber pressure generally resulted in a lower deposition rate. Film stress, as plotted and recorded against pressure, also matched general trends found with similar elements on other sputtering tools under different conditions. The key finding of this research was the consistency of these trends. The results suggest that the trends in film stress are element-specific and predictable. This research provides a foundation for future studies, allowing researchers to more accurately predict and plan for the effects of deposition parameters when working with novel materials.

Summary of Research:

Sputtering is a common deposition technique used to create the thin films necessary for building devices. Materials are selected based on their desired electrical, physical, or chemical properties. To ensure these desired effects are achieved, a standard table of characterization data is crucial, especially since sputtering tools can differ from each other even under "identical" conditions. Additionally, secondary effects like film stress are key considerations, as they can lead to device or film failure.

This research focused on collecting comprehensive data for a set of new materials on the AJA 1 and AJA 2 sputtering machines. The experimental process involved the following steps:

1. Wafer Preparation: Wafers underwent a MOS clean to remove organic contaminants and unwanted metals.

2. Native Oxide Removal: Prior to deposition, wafers were submerged in a two-minute buffered oxide etch to remove the native oxide layer.

3. Deposition: Experimental conditions were varied, with deposition times estimated to achieve a target thin-film thickness of 100-300 nm.

4. Data Collection: A patterned chip, or "witness sample," was attached to the carrier during deposition. After liftoff, a profilometer was used to measure the film height, assuming uniform deposition. This data was then used to measure film stress using a Flexus tool. Additional measurements were taken using a four-point probe for sheet resistance and an ellipsometer for refractive index.

Conclusions and Future Steps:

Analysis of the data reveals consistent trends between sputtering pressure and the resulting film properties, particularly for deposition rate and film stress. For most materials, an increase in chamber pressure correlated with a decrease in deposition rate, a widely observed phenomenon in sputtering processes. Similarly, film stress exhibited predictable, element-specific responses to pressure changes, with a clear shift from tensile to compressive stress in several cases (e.g., Zr, Nb) and a general trend of becoming less compressive with increasing pressure (e.g., Si3N4, Hf, Ti). These consistent, predictable trends suggest that film properties can be reliably tuned by controlling chamber

Material	Sputtering Machine	Pressure (mTorr)	Avg Height (A)	Time (s)	Deposition Rate (A/s)	Stress (MPa)	Stress Type	Avg Sheet Resistance(Ohm/sq)	Resistivity (μOhm * m)	Refractive Index	Box #	Wafer #
Zr	1	3Uncleaned	1490	1000	1.49	147.0	Tensile	9.39	1.3989312	N/A	1	1
Zr	1	3	1391	1000	1.39	-34.5	Compressive	7.74	1.07627234	N/A	1	2
Zr	1	7	1502	1000	1.50	-500.9	Compressive	46.93	7.0482852	N/A	1	3
Zr	1	20	1124	1000	1.12	-257.6	Compressive	427.57	48.058868	N/A	1	4
Al2O3	1	3	472	2000	0.24	-273.4	Compressive	Invalid	Invalid	1.60	1	5
Al2O3	1	7	1295	4000	0.32	-286.1	Compressive	Invalid	Invalid	1.63	1	6
Al2O3	1	20	668	4000	0.17	8.2	Tensile	Invalid	Invalid	1.63	1	7
Al2O3	1	3	1395	4000	0.35	-304.1	Compressive	Invalid	Invalid	1.66	1	8
Nb	1	3	1571	1800	0.87	619.7	Tensile	1.40	0.21957867	N/A	2	6
Nb	1	7	2020	1800	1.12	-248.3	Compressive	12.95	2.615092	N/A	2	7
Nb	1	20	1964	1800	1.09	-89.3	Compressive	92.81	18.2276876	N/A	2	8
SiN4	1	3	1528	2500	0.61	-490.5	Compressive	Invalid	Invalid	1.93	2	13
SiN4	1	7	1575	2500	0.63	-51.0	Compressive	Invalid	Invalid	1.62	2	14
SiN4	1	20	931	2500	0.37	-6.4	Compressive	Invalid	Invalid	1.57	2	15
Ti	1	3	1808	1500	1.21	151.5	Tensile			N/A	2	22
Ti	1	7	2284	1750	1.31	63.4	Tensile	20.88	4.7683068	N/A	2	17
Ti	1	20	2695	3600	0.75	38.7	Tensile	30.38	8.186871	N/A	2	18
Al	2	3	1887	1000	1.89	-35.9	Compressive	0.21	0.03878624	N/A	2	19
Al	2	7	1617	1200	1.35	-19.9	Compressive	0.32	0.051009882	N/A	2	20
Al	2	20	1613	2500	0.65	-44.7	Compressive	0.45	0.072481768	N/A	2	21
Hf	1	3	2134	1200	1.78	-2669.2	Compressive	4.60	0.98221618	N/A	3	1
Hf	1	7	1114	600	1.86	-808.3	Compressive	8.68	0.966651222	N/A	3	6
Hf	1	20	2915	1200	2.43	-71.0	Compressive	43.35	12.636525	N/A	3	7
NiO	1	3	1546	4000	0.39	-436.7	Compressive		0		3	10
NiO	1	7	1576	4000	0.39	-25.1	Compressive		0		3	11
NiO	1	20	799	4000	0.20	-122.1	Compressive		0		3	12
Ti	2	3	1471	1500	0.98	159.6	Tensile	6.68	0.98289278	N/A	3	13
Ti	2	7	1645	1750	0.94	30.0	Tensile	17.58	2.8917455	N/A	3	14
Ti	2	20	1686	3600	0.47	38.9	Tensile	28.47	4.7998734	N/A	3	15
Ru	2	3	2345	1000	2.35	-509.3	Compressive	0.54	0.125938225	N/A	2	2
Ru	2	7		1000	0.00				0	N/A	2	
Ru	2	20	3499	1000	3.50	-3.6	Compressive	19.87	6.9528629	N/A	2	5

Figure 1.

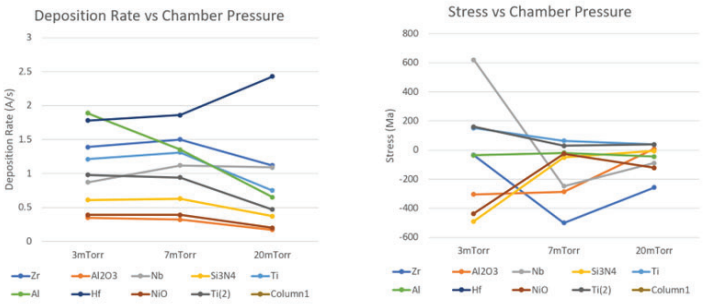

Figure 2.

pressure. The findings not only validate established sputtering principles but also provide a critical starting point for future researchers to optimize deposition conditions for a wide range of materials. In the future, this research hopes to expand its characterization by looking at film uniformity and roughness.

Acknowledgements:

Special thanks to Tom Pennell and the CNF staff for their support and mentorship throughout this whole research experience. I would like to acknowledge the CNF and their generosity for still offering a program after the 2025 AEOP program was canceled. This work was funded by the National Science Foundation via grants no. NNCI-2025233

Probing Spin Dynamics in Exfoliated van der Waals Ferromagnet Fe_5GeTe_2 Using Superconducting Resonators

CNF Summer Student: Matthew Willard
Student Affiliation: Physics, SUNY Geneseo

Summer Program(s): 2025 Cornell NanoScale Facility Research Experience for Undergraduates (CNF REU) Program, SUPREME REU

Principal Investigator(s): Gregory D. Fuchs

Mentor(s): Julie Soho Shim

Primary Source(s) of Research Funding: National Science Foundation award NNCI- 2025233, Center for Energy Efficient Magnonics (DE-AC02- 76SF00515), Department of Energy Office of Science, Basic Energy Sciences (DE-SC0019997)

Contact: gdf9@cornell.edu, jss545@cornell.edu, mtw14@geneseo.edu

Summer Program Website(s): https://cnf.cornell.edu/education/reu

Primary CNF Tools Used: AJA Orion Sputtering Systems, Heidelberg MLA 150 Maskless Aligner, Oxford 81/82, PT770 Etcher, DISCO Dicing Saw, Westbond 7400A Ultrasonic Wire Bonder

Abstract:

Two-dimensional (2D) magnetic materials offer a rich landscape for exploring spin dynamics and topological textures, with tunable properties and compatibility with heterostructure engineering. Among these, a 2D ferromagnet Fe_5GeTe_2 (F5GT) has emerged as a promising candidate due to its high Curie temperature and low Gilbert damping. However, bulk measurements are often limited by structural inhomogeneities. Here, we present a single-flake ferromagnetic resonance (FMR) study of exfoliated F5GT nanoflakes using high-Q superconducting resonators ($Q > 10^4$) to probe intrinsic damping properties with enhanced sensitivity. We observed ferromagnetic resonance in an F5GT flake transferred onto a 4 GHz superconducting resonator, demonstrating magnetic coupling between the flake and the resonator. The extracted upper bound for the Gilbert damping parameter is slightly lower than bulk values, indicating reduced damping in exfoliated samples. To further resolve damping contributions, we have also fabricated quarter-wavelength resonators with overtone modes and Q-factors exceeding 10^6, enabling frequency-resolved separation of viscous and inhomogeneous linewidth broadening. This work can offer new insights into the dynamical properties of van der Waals magnets.

Experimental Procedure:

Two-dimensional (2D) magnets have garnered significant attention for hosting exotic magnetic phenomena and topological spin textures, arising from strongly enhanced intrinsic spin fluctuations [1]. Their magnetic properties are readily tunable through external fields, strain, or chemical modifications, and their cleavable nature enables seamless integration into engineered heterostructures [1]. These features position 2D magnets as versatile platforms for probing fundamental spin interactions and developing multifunctional devices that integrate electronic, optical, and magnetic properties. Despite their intriguing properties, many two-dimensional ferromagnetic materials exhibit Curie temperatures significantly below room temperature, restricting their practical use. Recently, a promising candidate—Fe_5GeTe_2 (F5GT)—has been identified [2], demonstrating a Curie temperature of up to 332 K in bulk [3] and 280 K in exfoliated thin flakes (~10 nm) [2]. A recent ferromagnetic resonance (FMR) study reported that bulk F5GT crystals exhibit effective Gilbert damping coefficient of $\alpha \approx 0.01$—comparable to permalloy (NiFe)—although the measurements revealed substantial inhomogeneous linewidth broadening beyond viscous (Gilbert) damping contributions [3].

To better assess the intrinsic damping properties, we perform FMR measurements at the single- flake level using exfoliated F5GT, which are expected to be more structurally pristine. For this purpose, we design and fabricate high-Q superconducting resonators ($Q > 10^4$) and transfer exfoliated F5GT flakes onto them, enabling sensitive detection of their dynamic magnetic response (Fig. 1).

Fabrication:

Niobium (Nb) films were sputtered onto high-resistivity Si (100) wafers using AJA Orion Sputtering Systems. Superconducting resonators were fabricated by patterning the Nb layer with the Heidelberg MLA 150 Maskless Aligner, followed by cleaning with Oxford 81/82 and dry etching using a PT770 Etcher. The patterned wafers were subsequently diced using a

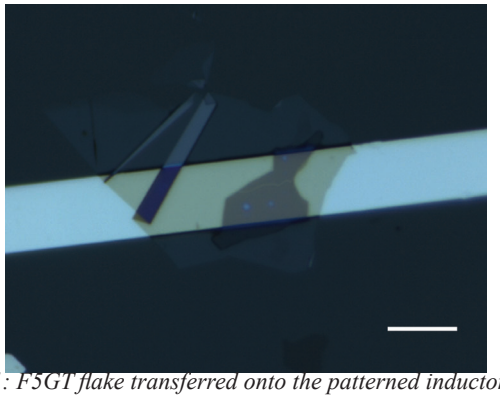

Figure 1: F5GT flake transferred onto the patterned inductor line of the 4 GHz superconducting resonator. A larger, close-to-transparent flake is the hBN flake capping the F5GT flake. The scale bar represents 10 µm.

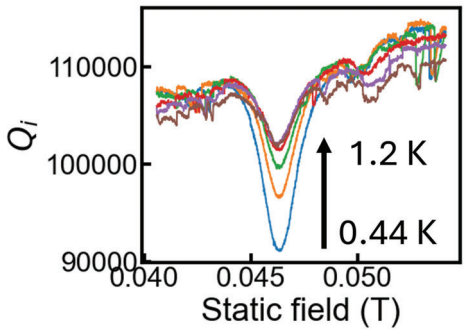

Figure 2: Ferromagnetic resonance (FMR) line at various temperatures.

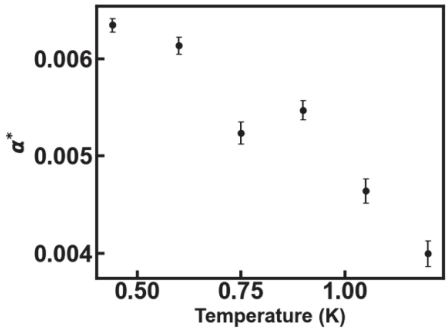

Figure 3: Estimated upper limit in Gilbert damping α at various temperatures..*

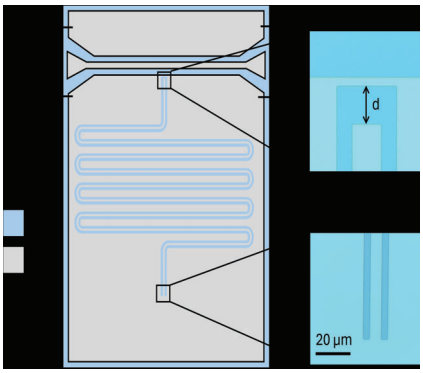

Figure 4: Schematic of the quarter-wavelength superconducting resonator. The zoomed-in optical images show the capacitive end and the inductive end of the resonator. The gap distance d in the capacitive end is 20 µm.

DISCO Dicing Saw. A nanoflake of Fe_5GeTe_2 (F5GT), capped with hexagonal boron nitride (hBN), was transferred onto the inductor line of the superconducting resonator (Fig. 1). For ferromagnetic resonance (FMR) measurements, the Westbond 7400A Ultrasonic Wire Bonder was used to wirebond the resonator to an electrical circuit component.

Conclusions and Future Steps:

We performed ferromagnetic resonance (FMR) measurements on a 25 nm F5GT flake capped with a 10 nm hBN flake that is transferred onto a 4 GHz lumped-element superconducting resonator. As shown in Fig. 2, we observe a decrease in the intrinsic Q-factor (Qi) at a static magnetic field of 0.046 T. This reflects that as the F5GT flake comes into resonance, it is drawing energy out of the superconducting resonator, which results in an apparent decrease in Qi. This measurement confirms the coupling between the flake and the resonator and demonstrates successful single- flake FMR detection.

To estimate an upper bound for the Gilbert damping parameter (α*), we analyze the FMR linewidth under the assumption of negligible inhomogeneous broadening. The extracted α* values are slightly lower but comparable to bulk values reported at 10 K (α ≈ 0.007), suggesting reduced damping in the exfoliated sample (Fig. 3). Interestingly, we observe that α decreases with temperature in the range of 0.4 – 1.2 K. To further investigate damping properties at the single-flake level, we have designed and fabricated quarter-wavelength superconducting resonators with optimized Q-factors, targeting values exceeding 106 (Fig. 4). A key advantage of this approach is that we will use the many overtone resonances, each as a separate frequency probe, which will allow us to distinguish viscous Gilbert damping from inhomogeneous linewidth broadening. The zoomed-in optical images show one representative device from a set of resonators we fabricated with varied gap distances, all of which are ready for FMR characterization. We plan to measure each resonator's Q-factor, transfer F5GT nanoflakes, and utilize overtone modes to extract the intrinsic damping parameters of F5GT with enhanced spectral resolution.

References:

[1] K. S. Burch, D. Mandrus, and J.-G. Park, Nature, 563, 47-52 (2018). J. M. Bartell, D. H. Ngai, Z. Leng, G. D. Fuchs, Nat. Commun., 6, 8460 (2015).

[2] A. F. May et al, ACS nano, 13, 4436-4442 (2019). C. Zhang, J. M. Bartell, J. C. Karsch, I. Gray, and G. D. Fuchs, Nano Lett., 21, 4966-4972 (2021).

[3] L. Alahmed et al, 2D Mater. 8, 045030 (2021).Mater. Quantum. Technol. 4(2), 025801 (2024).https://doi.org/10.1088/2633-4356/ad4b8c

[4] 1 M.P. Bland, F. Bahrami, J.G.C. Martinez, et al. "2D transmons with lifetimes and coherence times exceeding 1 millisecond," (2025).

Characterization of the Heidelberg MLA 150

CNF Summer Student: Jason Xu
Student Affiliation:

Summer Program(s): 2025 Summer CNF NORDTECH Intern

Mentor(s): Giovanni Sartorello , Cornell NanoScale Science and Technology Facility, Cornell University

Primary Source(s) of Research Funding: National Science Foundation under Grant No. NNCI-2025233, The Northeast Regional Defense Technology Hub

Contact: tjp83@cornell.edu, jasonxu810@gmail.com

Research Group Website: https://www.nordtechub.org

Primary CNF Tools Used: AJA Q, AJA Q2, Filmetrics R50, FleXus Film Stress Measurement, Hamatech Hot Piranha, P-7 Profilometer, Veeco Icon AFM

Abstract:

This research on the Heidelberg MLA 150 focuses on three key areas to optimize its performance: Dose and Defocus Tests, Alignment Tests, and Resist Characterization. The Dose and Defocus Tests aim to identify the ideal energy (dose) and laser optics position (defocus) for machine operation, with particular emphasis on regularly monitoring and correcting defocus drift caused by software malfunctions or stage crashes. Alignment Tests verify the functionality of the machine's internal alignment system by assessing the precision with which the laser writes complimentary patterns based on camera-read substrate patterns. Any misalignments are quantified, and correction factors are calculated. Finally, Resist Characterization involves empirically determining optimal exposure doses for various resists, populating a database that future users can access for efficient and accurate material processing.

Summary of Research:

My research on the Heidelberg MLA 150 has been focused around three main tests/areas: Dose and Defocus Tests, Alignment Test, and Resist Characterization. The purpose of Dose and Defocus Tests is to determine the optimal Dose and Defocus for the machine to operate. Dose is a measure of the nominal energy used to expose the substrate, while defocus is a measure of the position of the machine's laser optics. We can determine the most optimal combination of dose and defocus by exposing test patterns at various dose and defocuses and reading the resolutions of the tests. Attention is focused on the Defocus, as it is much more likely to drift due to software malfunctions and stage crashes. As a result of these crashes, Dose and Defocus Tests must be carried out regularly to ensure that the optimal dose and defocus values are known. The purpose of Alignment Tests is to ensure that the alignment system within the machine is working properly, by loading a substrate that contains patterns spread around that may be read by a camera within the machine. The camera sends the information to the alignment system, which relays to the laser where it believes the substrate and staging is, which then writes a complimentary pattern to the original pattern on the substrate. We read how well the two patterns fit together, which tells us whether the alignment system is working properly [2]. Oftentimes, the alignment is not perfect, and we are able to calculate a correction factor to input into the machine by reading the offsets of the patterns. The rest of the time on the Heidelberg MLA 150 was spent on Resist Characterization. By testing a large range of doses on various resists, we were able to determine the optimal doses for many resists that we add to a database that future users may access and quickly determine the optimal dose to expose at.

Conclusions and Future Steps:

Dose and Defocus Tests and Alignment Tests must be regularly conducted due to stage crashes and other natural shifts. These ensure that users are always exposing at the most optimal dose and defocus and that the alignment system is working properly. Besides these tests, the database for Resist Characterization may always be added upon, and future time should be spent characterizing a larger selection of resists.

Acknowledgements:

Special thanks go out to Giovanni Sartorello for his support and mentorship throughout this internship. I would also like to acknowledge the Cornell NanoScale Facility for hosting this experience. This work was funded by a grant from NORDTECH.

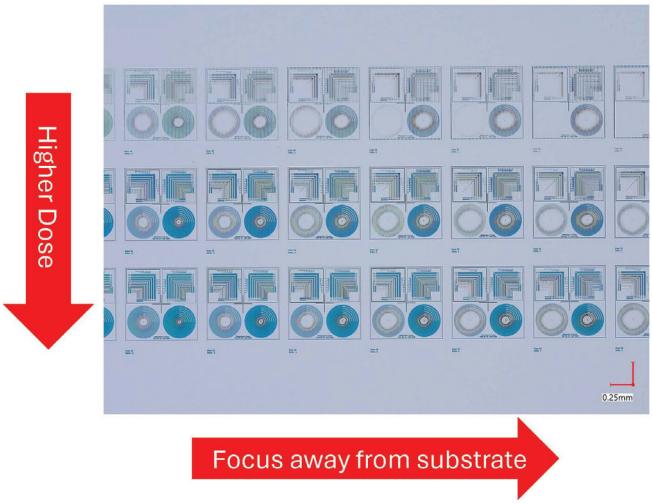

Figure 1: Dose and Defocus Test on a Wafer Coated in S1805.

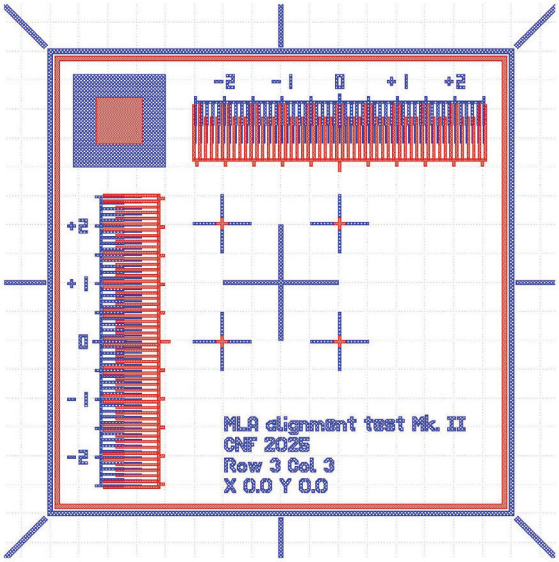

Figure 2: Alignment Test gds File.

Effects of Reactive Ion Etching on Conductivity of NbAs

CNF Summer Student: Iris You
Student Affiliation: Department of Materials Science and Engineering, Rutgers University

Summer Program(s): 2025 Cornell NanoScale Facility Research Experience for Undergraduates (CNF REU) Program, SUPREME REU

Principal Investigator(s): Judy J. Cha, Department of Materials Science and Engineering, Cornell University

Mentor(s): Yeryun Cheon, Department of Physics, Cornell University

Primary Source(s) of Research Funding: National Science Foundation under Grant No. NNCI-2025233, SUPREME Research Experience for Undergraduates #2349310

Contact: jc476@cornell.edu, yc2458@cornell.edu, icy2@scarletmail.rutgers.edu

Summer Program Website(s): https://cnf.cornell.edu/education/reu

Primary CNF Tools Used: Veeco Icon AFM, PT 720-740 RIE, Zeiss Supra SEM, Zeiss Ultra SEM

Abstract:

The continuation of Moore's Law has resulted in persistent downscaling of transistors and current copper (Cu) interconnects resulting in performance bottlenecks when interconnect dimensions are below the electron mean free path (~40 nm) of Cu [1]. Since Cu exhibits high resistance at such dimensionsscales, resistance-capacitance (RC) signal delay and high-power consumption result in lower overall performance [1]. Topological semimetals possess topologically protected conducting surface states that result in low resistivity at low dimensions [2]. Thus, they are of interest in the discovery of novel materials to replace Cu interconnects.

One such material is the Weyl semimetal niobium arsenide (NbAs). We have shown single crystal NbAs nanowires, produced by nanomolding, which has previously been shown to possess conductivity comparable to that of Cu at desirable length scales [3]. However, the promising resistivity trends of NbAs must be studied further as a function of size at sizes between these 10 nm and bulk crystals. has not been extensively studied aIn addition, nd the effects of surface damage on conductivity due to various processing techniques has not been reported must be explored.

In this work, we use reactive ion etching (RIE) to reduce the size of focused ion beam (FIB) produced NbAs nanoscale samples prepared by focused ion beam (FIB) milling and examine the trends in resistivity as a function of NbAs size and RIE conditions. We show that NbAs can be etched roughly linearlycontrollably and reliably under mild RIE conditions and resistivity continuously decreases as NbAs is reduced in size. This allows for greater understanding of resistivity scaling and its mechanisms in NbAs.

Summary of Research:

We etched fabricated single crystal NbAs nanoslabs using FIB milling and created electrical devices. A completed device is shown in Figure 1. Length and width measurements were extracted from scanning electron microscopy (SEM) images. Atomic force microscopy (AFM) was used to measure the height of the slabs. The cross-sectional area of the slabs was calculated from this data. Resistance measurements were acquired via 4-point probe current and voltage measurements. The measured resistance was converted to resistivity When combined with dimensional data, we were able to calculate the resistivity of our NbAs slabsfor the NbAs slabs.

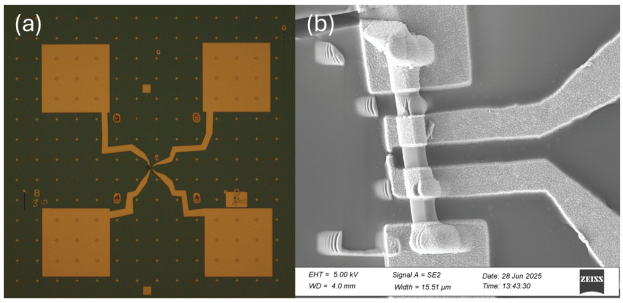

Figure 1: (a) Optical image of NbAs Device 3. (b) SEM image of Device 3.

The slabs were successively etched with RIE at 10 mTorr with 60 W of power using 30 sccm Cl_2 and 10 sccm CF_4 at varying etching times. Afterwards, AFM and resistance measurements were repeated to observe the changes in height and resistivity of the slabs. Figure 2 shows how uncertainty in the height measurements and thus etching calibration occurs due to the shape of the AFM tip as well as the geometry of the sample placed on the substrate. Additionally, we take into accountconsider the etching of the substrate when calculating the effects of etching. Overall, we are able to etched our devices at approximately 5-7 nm per minute.

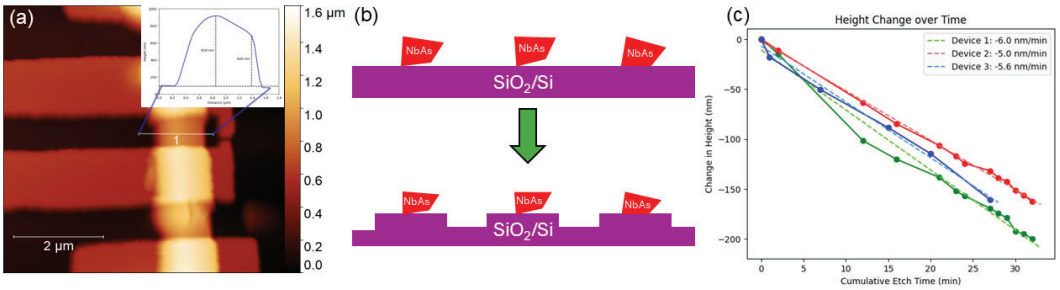

Figure 2: (a) AFM image with height profile of Device 3 pre-etching. (b) Schematic showing etching of substrate layer during RIE. (c) Plot of NbAs height change with respect to etching time.

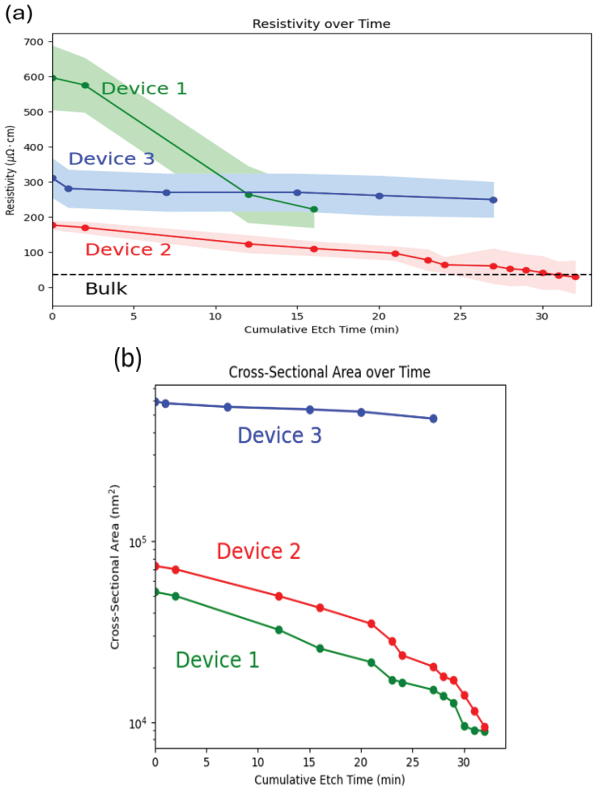

Figure 3: (a) Resistivity of NbAs devices as a function of total etch time. (b) Cross-sectional area of nanoslabs as a function of etch time.

There is a clear decreasing trend in resistivity as a function of cumulative etching time as shown in Figure 3. This supports the resistivity scaling trend of NbAs, and as the surface to volume ratio continuously increases from etching, the resistivity eventually falls below the bulk value while still decreasing.

SEM images in Figure 4 show considerable surface damage from RIE on the surface of the NbAs nanoslabs. However, the overall conductivity of the samples continues to exhibit decreasing behavior despite the surface damage.

Conclusions and Future Steps:

We progressively etched NbAs nanoslab devices through RIE at an etching rate of approximately 5-7 nm/min. We were further able to show that RIE is effective in reducing the size of NbAs without adversely affecting conductivity. We confirmed promising trend of decreasing resistivity for NbAs at decreasing dimensions in the nanoscale regime.

Future work would involve improving height measurements which are currently overestimated due to the geometry of the sample and FIB placement. Better methods to measure cross-sectional area would result in less overall error and a clearer understanding of our results. We would also like to continue investigating the surface contributions to the resistivity scaling of NbAs with RIE etching in future devices and investigate even less destructive methods of size reduction, whether it be through RIE or other means.

References:

[1] Joon-Seok Kim et al., Addressing interconnect challenges for enhanced computing performance. Science 386, eadk6189 (2024). DOI:10.1126/science.adk6189

[2] Asir Intisar Khan et al., Surface conduction and reduced electrical resistivity in ultrathin noncrystalline NbP semimetal. Science 387,62-67(2025). DOI:10.1126/science.adq7096

[3] Cheon, Y et al. https://arxiv.org/abs/2503.04621 (2025).

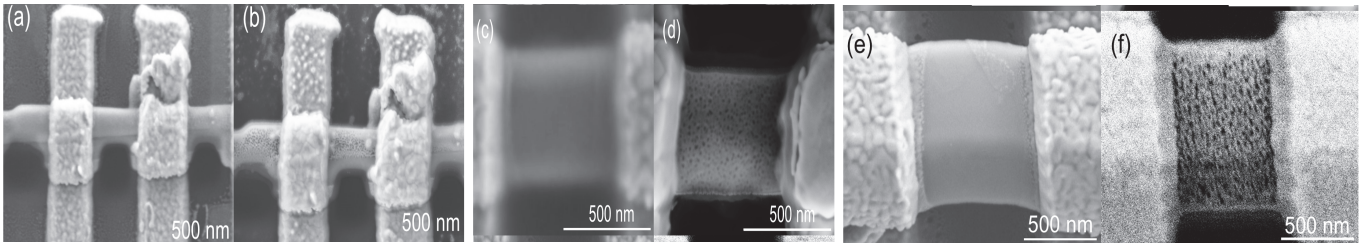

Figure 4: (a) Pre-etch SEM of Device 1. (b) Post-etch SEM of Device 1. (c) Pre-etch SEM of Device 2. (d) Post-etch SEM of Device 2. (e) Pre-etch SEM of Device 3. (f) Post-etch SEM of Device 3.

CNF

Cornell NanoScale
Science and Technology Facility